JGR Solid Earth

RESEARCH ARTICLE
10.1029/2022JB025072

Hydrothermal Friction Experiments on Simulated Basaltic Fault Gouge and Implications for Megathrust Earthquakes

Hanaya Okuda[1,2], André R. Niemeijer[3], Miki Takahashi[4], Asuka Yamaguchi[1,2], and Christopher J. Spiers[3]

[1]Department of Ocean Floor Geoscience, Atmosphere and Ocean Research Institute, University of Tokyo, Kashiwa, Japan, [2]Department of Earth and Planetary Science, University of Tokyo, Bunkyo, Japan, [3]Department of Earth Sciences, Utrecht University, Utrecht, The Netherlands, [4]Research Institute of Earthquake and Volcano Geology, Geological Survey of Japan, National Institute of Advanced Industrial Science and Technology, Tsukuba, Japan

Key Points:

- Altered basalt shows unstable frictional behavior under a wide range of hydrothermal conditions
- Production of fine-grained albite during subduction promotes the frictional instability via pressure solution creep
- Subducting oceanic crust may serve as a source of nucleating megathrust earthquakes in subduction zones

Supporting Information:

Supporting Information may be found in the online version of this article.

Correspondence to:

H. Okuda and A. R. Niemeijer,
okuda@aori.u-tokyo.ac.jp;
A.R.Niemeijer@uu.nl

Citation:

Okuda, H., Niemeijer, A. R., Takahashi, M., Yamaguchi, A., & Spiers, C. J. (2023). Hydrothermal friction experiments on simulated basaltic fault gouge and implications for megathrust earthquakes. *Journal of Geophysical Research: Solid Earth*, *128*, e2022JB025072. https://doi.org/10.1029/2022JB025072

Received 30 JUN 2022
Accepted 17 DEC 2022

Author Contributions:

Conceptualization: Hanaya Okuda, Asuka Yamaguchi
Data curation: Hanaya Okuda, André R. Niemeijer
Formal analysis: Hanaya Okuda
Funding acquisition: Hanaya Okuda, André R. Niemeijer, Asuka Yamaguchi
Investigation: Hanaya Okuda
Methodology: Hanaya Okuda, André R. Niemeijer, Miki Takahashi
Resources: Hanaya Okuda, André R. Niemeijer, Miki Takahashi, Asuka Yamaguchi, Christopher J. Spiers

Abstract Nucleation of earthquake slip at the plate boundary fault (décollement) in subduction zones has been widely linked to the frictional properties of subducting sedimentary facies. However, recent seismological and geological observations suggest that the décollement develops in the subducting oceanic crust in the depth range of the seismogenic zone, at least in some cases. To understand the frictional properties of oceanic crustal material and their influence on seismogenesis, we performed hydrothermal friction experiments on simulated fault gouges of altered basalt, at temperatures of 100–550°C. The friction coefficient (μ) lies around 0.6 at most temperature conditions but a low μ down to 0.3 was observed at the highest temperature and lowest velocity condition. The velocity dependence of μ, ($a-b$), changes with increasing temperature from positive to negative at ∼100°C and from negative to positive at ∼450°C. Compared to gouges derived from sedimentary facies, the altered basalt gouge showed potentially unstable velocity weakening over a wider temperature range. Microstructural observations and microphysical interpretation infer that competition between dilatant granular flow and viscous compaction through pressure-solution creep of albite contributed to the observed transition in ($a-b$). Alteration of oceanic crust during subduction produces fine grains of albite and chlorite through interactions with interstitial water, leading to reduction in its frictional strength and an increase in its seismogenic potential. Therefore, shear deformation possibly localizes within the altered oceanic crust leading to a larger potential for the nucleation of a megathrust earthquake in the depth range of the seismogenic zone.

Plain Language Summary Megathrust earthquakes in subduction zones have long been studied to mitigate damage by ground shakings and tsunamis. Frictional properties of plate boundary fault are fundamental information to understand the slip activities causing megathrust earthquakes. In this study, we focused on altered basalt, which is a rock of subducting oceanic crust and has not been focused on as much as sedimentary rocks. Laboratory friction experiments were performed at a wide temperature range with water pressurized conditions. We found that the altered basalt shows frictionally unstable behavior of the type that is prerequisite for generating an earthquake in the temperature conditions of seismogenic zone. This unstable behavior is likely to be result of alteration of oceanic crust during subduction. Because the altered basalt can be mechanically as weak as sedimentary facies, subducting oceanic crust forms an additional or perhaps even preferred candidate for sourcing megathrust earthquakes in subduction zones.

1. Introduction

Megathrust earthquakes in subduction zones generally source in the depth range of ∼5–25 km corresponding to a temperature (T) range of ∼150–350°C (Hyndman et al., 1997). The extent of this "seismogenic zone" was originally postulated to be related to the smectite-illite dewatering transition as the transition temperature is consistent with the temperature condition at the up-dip limit of the seismogenic zone (Oleskevich et al., 1999). However, this hypothesis is not fully supported by experiments (e.g., Saffer & Marone, 2003). Instead, recent experimental studies showed that the effect of temperature on the velocity dependence of illite-quartz mixture can explain both up-dip and down-dip limits (Den Hartog, Peach, et al., 2012), and that a change in the extent of lithification of sediments during subduction may contribute to making the plate boundary fault (décollement) frictionally unstable (Ikari & Hüpers, 2021).

Supervision: André R. Niemeijer, Miki Takahashi, Asuka Yamaguchi, Christopher J. Spiers
Visualization: Hanaya Okuda
Writing – original draft: Hanaya Okuda
Writing – review & editing: André R. Niemeijer, Miki Takahashi, Asuka Yamaguchi, Christopher J. Spiers

The frictional properties of sediments have long been the focus for understanding the frictional behavior of the décollement. This approach is certainly valid for shallow depths near the trench, where sedimentary décollement materials have been successfully drilled from the plate boundary, for example, in the Japan Trench, NE Japan, in relation to the 2011 Tohoku-oki Earthquake (Chester et al., 2013) or in the Nankai Trough, SW Japan (Sakaguchi et al., 2011). However, subducting oceanic crust, that is, basalt and altered basalt, are likely to play an important role in some convergent margins, specifically where the décollement may sometimes step down into the oceanic crust or into the interface between the oceanic crust and overlying sediment—as in the Nankai Trough and the Sagami Trough (H. Kimura et al., 2010; Park et al., 2002). Such down-stepping is evident in seismic reflection data and from geological observations of underplated basaltic layers found in exhumed accretionary complexes all over the world (Figure 1) (G. Kimura & Ludden, 1995; Kusky et al., 2013; Wakita, 2015). The basaltic layers found in the Shimanto complex experienced temperatures of 150–300°C (Kameda et al., 2017). Similarly, those in Franciscan complex experienced 200–250°C (Meneghini & Moore, 2007), those in Alaska experienced 250–300°C (Braden & Behr, 2021), and those found in the Chrystalls Beach complex experienced temperature up to 300°C (Fagereng & Cooper, 2010). These temperature conditions match the seismogenic zone depth in subduction zones, suggesting that the frictional properties of subducting basaltic layers derived from the oceanic crust could play an important role in seismogenesis. However, experimental studies on basaltic fault rock of the type found in subduction zones, and under subduction zone conditions, are limited.

It is well established that oceanic crust commonly experiences partial alteration soon after its formation, because of the interaction between mid-ocean ridge (fresh) basalt and interstitial water (Braden & Behr, 2021; Kameda et al., 2017; Phillips et al., 2019; Ujiie et al., 2007). At shallow depths, such as the current seafloor, the volcanic glass component alters into saponite, which is an Mg-rich smectite (Kameda et al., 2011). As the altered oceanic crust later subducts, saponite dehydrates to form chlorite at ∼150°C (Kameda et al., 2011). At a similar temperature, albitization of anorthic plagioclase also occurs (Moore et al., 2007), which also produces chlorite (Rosenbauer et al., 1988). The mineral assemblage present in altered basalt up to ∼300°C is accordingly ∼25% saponite or chlorite, ∼25% clinopyroxene, and ∼50% plagioclase (Kameda et al., 2017). At temperatures >300°C, clinopyroxene decomposes into epidote and quartz (Kameda et al., 2017) or actinolite (and quartz) (Humphris & Thompson, 1978; Takeshita et al., 2015).

In previous room temperature studies (Ikari et al., 2020), unaltered basalt gouge under 25 MPa effective normal stress (σ_n^{eff}) with 5 or 24 MPa pore pressure (P_f) conditions exhibited velocity-neutral to velocity-weakening behavior at slip velocities of 3–300 μm/s, whereas altered basalt gouge showed a clear trend toward more frictionally stable behavior with increasing velocity (>3 μm/s). Velocity-weakening behavior was observed only at low velocities (<1 μm/s) in the case of surface sliding of altered basalt with saponite, suggesting that the altered basalt is capable of hosting slow slip events at shallow depths (Ikari et al., 2020). At elevated T conditions, unaltered basalt gouge under ∼50 MPa σ_n^{eff} with 100 MPa P_f showed velocity-weakening behavior in the range of T = 250–600°C and at shearing velocities of 0.02–1.15 μm/s (Zhang et al., 2017). Altered basalt with chlorite has only been tested under hydrothermal conditions at T = 150°C with confining pressure of 120 MPa and 43 or 84 MPa P_f, showing velocity-weakening behavior (Phillips et al., 2020). Friction coefficients of unaltered and altered basalt are 0.6–0.7 at T = 150°C, higher than those of illite-rich shale (range 0.45–0.55) (Den Hartog, Niemeijer, et al., 2012; Phillips et al., 2020). Mixed actinolite-chlorite and chlorite gouges also show velocity-weakening behavior at T = 200–400°C and 300°C, respectively (Okamoto et al., 2019, 2020). In addition, a low σ_n^{eff} (<50 MPa) is reported to promote velocity-weakening behavior in the case of blueschist gouge sheared at T = 22–400°C under $P_f = \sigma_n^{eff}$ conditions (Sawai et al., 2016). These studies imply that subducting altered oceanic crustal material has the potential to exhibit unstable frictional behavior, but the dependencies of its frictional stability on T, P_f, and σ_n^{eff} are not yet fully understood.

In this study, we collected altered basaltic rock from an exhumed mélange in SW Japan and conducted friction experiments on a simulated gouge prepared from it at temperatures ranging from 100°C to 550°C. The aim was to investigate the frictional behavior of subducting oceanic crustal material under the conditions of the seismogenic zone. We mostly used an σ_n^{eff} of 100 MPa and P_f of 100 MPa, and independently tested the effects of increasing P_f and reducing σ_n^{eff} on frictional behavior.

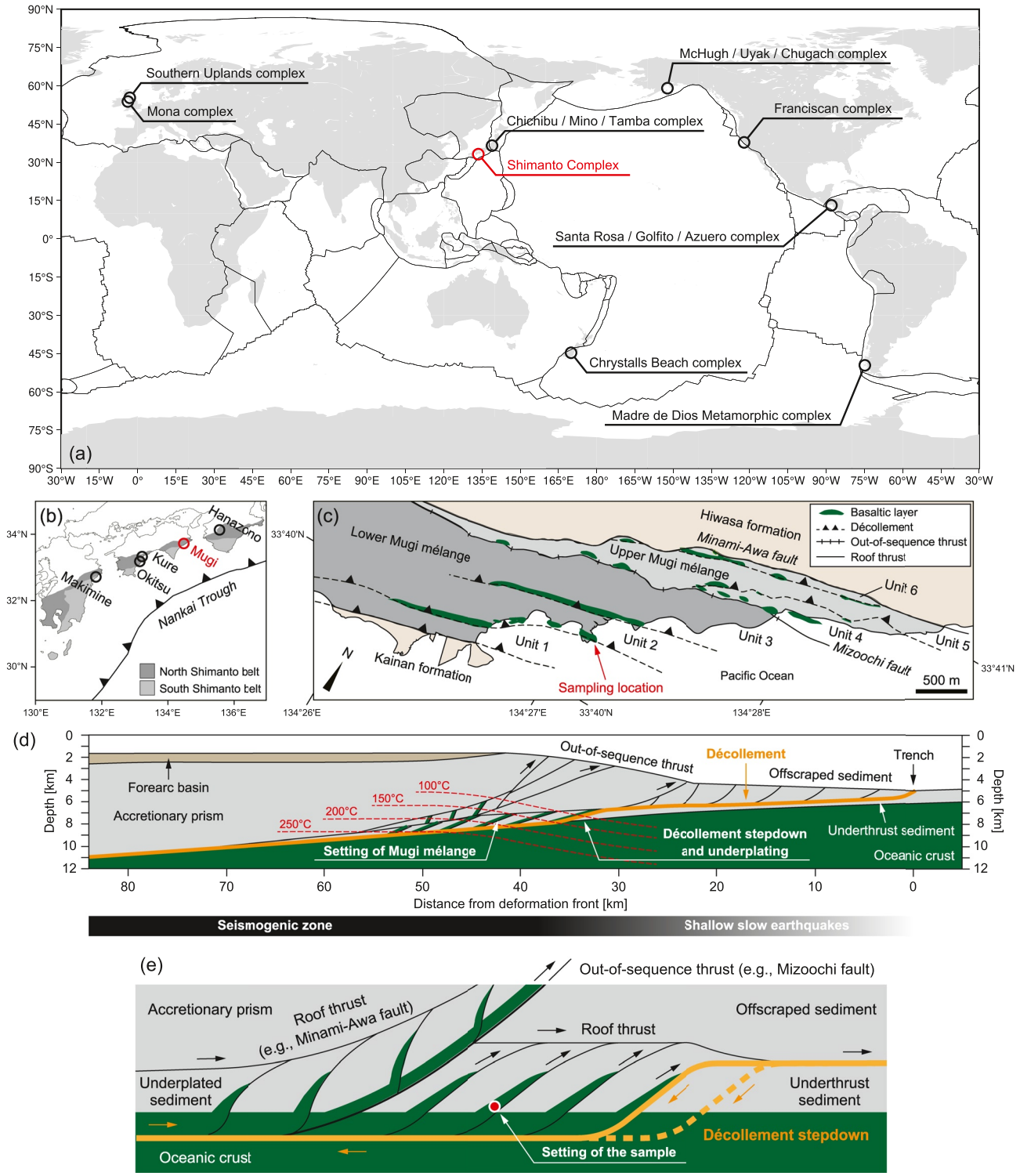

Figure 1.

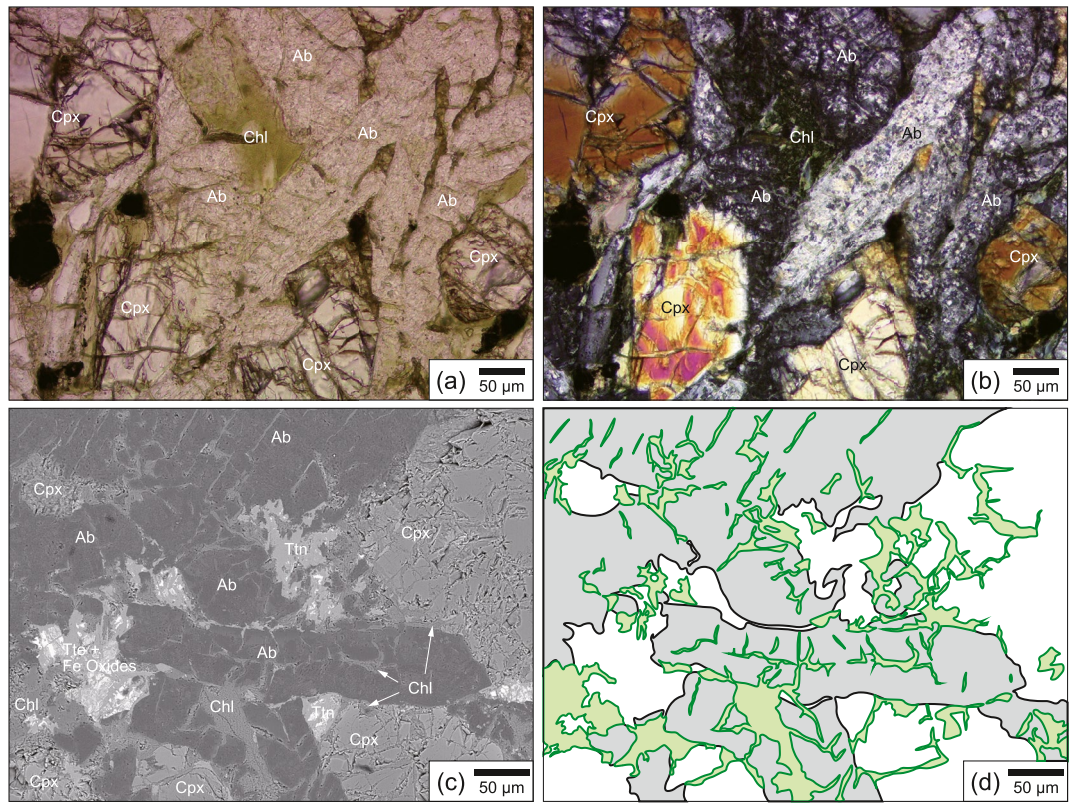

Figure 2. Microstructures of intact altered basalt sample under plane-polarized (a), crossed-polarized (b), and BSE images (c). (d) Albite (gray areas) and chlorite (green areas) distributions based on (c). Mineral identification is based on EDS analysis. Ab: albite; Cpx: clinopyroxene; Chl: chlorite; Ttn: titanite.

2. Method

2.1. Samples

The altered basalt sample used in this study was collected from an outcrop of the Mugi mélange, in the Shimanto accretionary complex, SW Japan (Figure 1b). This mélange formed in the Late Cretaceous and experienced temperatures (T) of 150–200°C, based on vitrinite reflectance data, and a pore pressure (P_f) of ~100 MPa, based on fluid inclusion geothermometry (Ikesawa et al., 2005; G. Kimura et al., 2012; Kitamura et al., 2005; Matsumura et al., 2003). The basalt initially formed as mid-ocean ridge basalt. This was subducted into the seismogenic zone of a former subduction plate boundary similar to the current Nankai Trough. It was then incorporated into the accretionary prism by underplating associated with décollement stepdown, and then exhumed (G. Kimura et al., 2012). The altered basalt sample is composed of albitized plagioclase, clinopyroxene, and chlorite (Figure 2). The albitized plagioclase consists of fine grains of albite with a grain size of about 10 μm (Figure 2b). Chlorite is formed within and around albitized plagioclase (Figure 2d). Before experimentation, we crushed and sieved the sample to obtain a simulated gouge material with a grain size of <100 μm. This initial grain size has little influence on frictional properties during steady state sliding, as the grain size in the gouge always becomes significantly reduced in the initial

Figure 1. (a) Global map showing examples of accretionary complexes where underplated ocean floor basalt or seamount basalts are found at relatively shallow depths (T < 300°C) (cf., G. Kimura and Ludden (1995); Kusky et al. (2013); Raymond (2019); Wakita (2015)). Shimanto complex in SW Japan (Kameda et al., 2017), Chichibu, Mino, Tamba complex in central Japan (G. Kimura & Ludden, 1995), Franciscan complex in California (Meneghini & Moore, 2007), McHugh, Uyak, Chugach complex in southern Alaska (Braden & Behr, 2021; Kusky & Bradley, 1999), Southern Uplands complex in Scotland (Leggett et al., 1979), Mona complex in Wales (Kawai et al., 2007; Maruyama et al., 2010), Chrystalls Beach complex in New Zealand (Fagereng & Cooper, 2010), Madre de Dios Metamorphic complex in southern Chile (Willner et al., 2009), Santa Rosa, Golfito, Azuero complex in Costa Rica and Panama (Baumgartner & Denyer, 2006; Buchs et al., 2010). (b) Mélanges where underplated basaltic layers are found in the Shimanto complex: Hanazono mélange (Onishi et al., 2001), Mugi mélange (Ikesawa et al., 2005; G. Kimura et al., 2012; Kitamura et al., 2005), Kure mélange (Mukoyoshi et al., 2006), Okitsu mélange (Ikesawa et al., 2003), and Makimine mélange (Hara & Kimura, 2008). (c) Closeup map view of Mugi mélange modified after Yamaguchi et al. (2012) showing the sampling location. (d) Schematic cross section of the Nankai Trough and (e) schematic cross section showing the geological structures of Mugi mélange where the décollement steps down into the oceanic crust (G. Kimura et al., 2012).

stages of deformation and associated shear localization (Marone & Scholz, 1989; Scuderi et al., 2017). The mineral composition of the sample was estimated by point counting ~1,300 grains in a thin section. We obtained ~50% albite, ~27% clinopyroxene, ~15% chlorite, and ~8% opaque minerals, which is generally consistent with previously reported compositions of basaltic rock from the Mugi mélange (Kameda et al., 2017; Phillips et al., 2020).

2.2. Experiments

Laboratory friction experiments were conducted on the simulated gouge material using the hydrothermal ring shear apparatus at Utrecht University (Figure 3). In preparing each experiment, 0.5 g of sample was sandwiched between two René-41 Superalloy pistons, confined laterally between an outer confining ring (diameter = 28 mm) and an inner confining ring (diameter = 22 mm). The gouge had a thickness of ~1.2 mm before imposing the normal load. The piston-sample assembly was subsequently placed inside the hydrothermal pressure vessel in line with the machine's pressure-compensated loading piston, allowing us to control both the effective normal stress (σ_n^{eff}) and pore pressure (P_f) independently. Distilled water was introduced into the pressure vessel as the pore fluid and the sample region heated using an internal furnace to achieve the desired temperature (T) conditions. Because the sample is not sealed by the outer/inner rings, pore fluid can freely access the sample. See previous studies for details of the apparatus (Den Hartog, Niemeijer, et al., 2012; Niemeijer et al., 2016).

Experiments were performed at a σ_n^{eff} of 100 MPa, a P_f of 100 MPa, and velocities (V) of 1-3-10-30-100 μm/s. Initial "run-in" shearing at 1 μm/s was imposed over 5 mm of shear displacement. Subsequent shear displacement was set to be 1.5 mm for V of 1–10 μm/s and 3 mm for 30 and 100 μm/s. Various T conditions from 100°C to 550°C were tested by stepping T by 50°C in the range 100-150-200-250°C for u968, 250-300-350-400°C for u972, and 400-450-500-550°C for u992 and u996 (see Table 1). We refer to each T, σ_n^{eff}, P_f condition in a given experiment as a "stage" (e.g., stage 1 for u968 was done under T = 100°C; Figure 3d). Changes in V at constant T were abruptly imposed, whereas we waited at least 1 hr after a change in T to allow the system to stabilize. To elucidate the effect of shear displacement on frictional behavior, tests at 250°C and 400°C were performed at varying displacements. At T = 200°C and 500°C, the effects of over-pressured conditions ($P_f > \sigma_n^{eff}$) were tested by varying P_f from 50 to 200 MPa and σ_n^{eff} from 30 to 100 MPa, independently. An additional experiment with V stepped in the range from 0.003 μm/s to 1 μm/s was performed specifically at T = 400°C to investigate the frictional behavior at a sliding velocity close to the plate convergence rate (e.g., 4–6.5 cm/year = 0.001–0.002 μm/s in the case of the Nankai Trough (Miyazaki & Heki, 2001; Seno et al., 1993)). Three "microstructural characterization experiments" were also performed for microstructural observations. Two experiments of the three were performed with constant velocity conditions (u980 with 1 μm/s and u981 with 100 μm/s) under T = 400 and 100°C, respectively. The other one experiment was initially deformed over 5 mm shear displacement with 1 μm/s followed by a single velocity step to 0.01 μm/s under T = 550°C (u975). Total shear displacements for all three microstructural characterization experiments were 8.7 mm. We also performed one test stepping the temperature from T = 100–200°C under vacuum dry condition (u1003) to see the effect of the absence versus presence of pore fluid (pressure) on frictional behavior. See Table 1 and Table S1 in Supporting Information S1 for the detailed experimental conditions.

2.3. Data Acquisition and Processing

During individual experiments, shear displacement, normal displacement, applied normal force, torque, temperature, and pore pressure signals were continuously logged at a sampling rate of 1–100 Hz. The raw data was converted to (effective) normal and shear stresses using the sensor calibrations and sample dimensions (see information in data repository). Friction coefficient μ was obtained from the shear stress normalized by the effective normal stress (σ_n^{eff}) without considering cohesion.

We found that the friction coefficient (μ) had a positive relation with shear displacement (Figure 3d, see also Figure 4a). Since we stepped temperature (T) at larger displacement (d), friction data at higher T were influenced by the displacement history (Figure 4b). To correct the effect of d, our experiments were designed to have the same T condition at different d for T = 250°C (stage 4 for u968 and stage 1 for u972) and 400°C (stage 4 for u972 and stage 1 for u992 and u996). Using the data with velocity (V) = 10 μm/s, which had less fluctuation than those with other V conditions, we obtained slip-hardening trends (μ/d) of 0.005 mm^{-1} for T = 250°C and 0.003 mm^{-1} for 400°C. Therefore, we used 0.004 mm^{-1} as a universal slip-hardening trend (gray line in Figure 4a) to obtain the first estimation of μ values with slip-hardening trend removed (Figure 3d, see also Figure 4b). The detrended

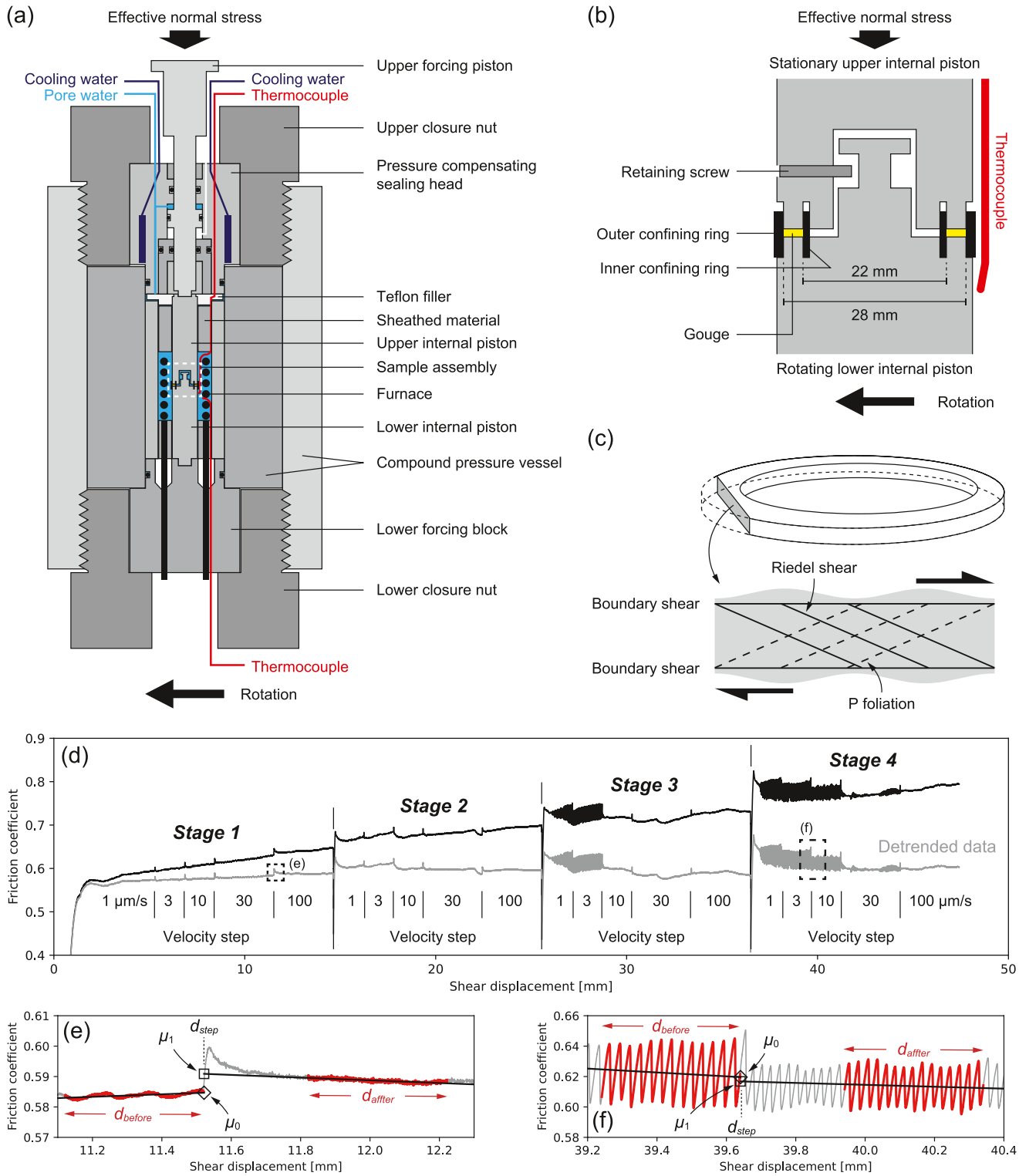

Figure 3. Schematic views of (a) the hydrothermal ring shear apparatus and (b) the close-up view of the sample assembly (Chen et al., 2020; Den Hartog, Niemeijer, et al., 2012). After the experiment, the sample was retrieved and microstructure was observed using the cross section shown in (c). (d) Overview of the velocity sequences and stages employed in this study (example of u968 with detrended data shown in gray). (e) and (f) Examples of *V*-steps. Red portions are the data used to obtain the local trends before and after the *V*-step, and black lines are the obtained local trends. Diamonds and squares in (e) and (f) show the μ-values before (μ_0) and after (μ_1) the *V*-step used to calculate $\Delta\mu_{ss}$. The $\Delta\mu_{ss}$ for the cases in (e) and (f) are 0.0062 ± 0.0001 and −0.0029 ± 0.0016, respectively. (f) Illustrates the stick slip case.

Table 1
List of Experiments and Corresponding Conditions

Run	Stage	T [°C]	σ_n^{eff} [MPa]	P_f [MPa]	V [μm/s]	d [mm]
u968	1	100	100	100	1-3-10-30-100	0–14.6
	2	150				14.6–25.6
	3	200				25.6–36.5
	4	250				36.5–47.4
u972	1	250	100	100	1-3-10-30-100	0–14.6
	2	300				14.6–25.6
	3	350				25.6–36.5
	4	400				36.5–47.4
u992	1	400	100	100	1-3-10-30-100	0–14.6
	2	450				14.6–25.6
	3	500				25.6–36.5
	4	550				36.5–47.4
u996	1	400	100	100	1-3-10-30-100	0–14.6
	2	450				14.6–25.6
	3	500				25.6–36.5
	4	550				36.5–47.4
u991	1	200	100	50	1-3-10-30-100	0–14.6
	2			100		14.6–25.6
	3			150		25.6–36.5
	4			200		36.5–47.4
u993	1	500	100	50	1-3-10-30-100	0–14.6
	2			100		14.6–25.6
	3			150		25.6–36.5
	4			200		36.5–47.4
u1002	1	200	30	100	1-3-10-30-100	0–14.6
	2		50			14.6–25.6
	3		100			25.6–36.5
	4		50			36.5–47.4
u1006	1	500	30	100	1-3-10-30-100	0–14.6
	2		50			14.6–25.6
	3		100			25.6–36.5
	4		50			36.5–47.4
u1003	1	100	100	Vacuum dry	1-3-10-30-100	0–14.6
	2	150				14.6–25.6
	3	200				25.6–36.5
u1017	1	400	100	100	1-0.003-0.01-0.03-0.1-0.3-1	0–10.6
u975	1	550	100	100	1–0.01	0–8.7
u980	1	400	100	100	1	0–8.7
u981	1	100	100	100	100	0–8.7

Note. T = temperature, σ_n^{eff} = effective normal stress, P_f = pore fluid pressure, V = velocity, and d = shear displacement. Stage refers to each T, σ_n^{eff}, and P_f condition in a given run.

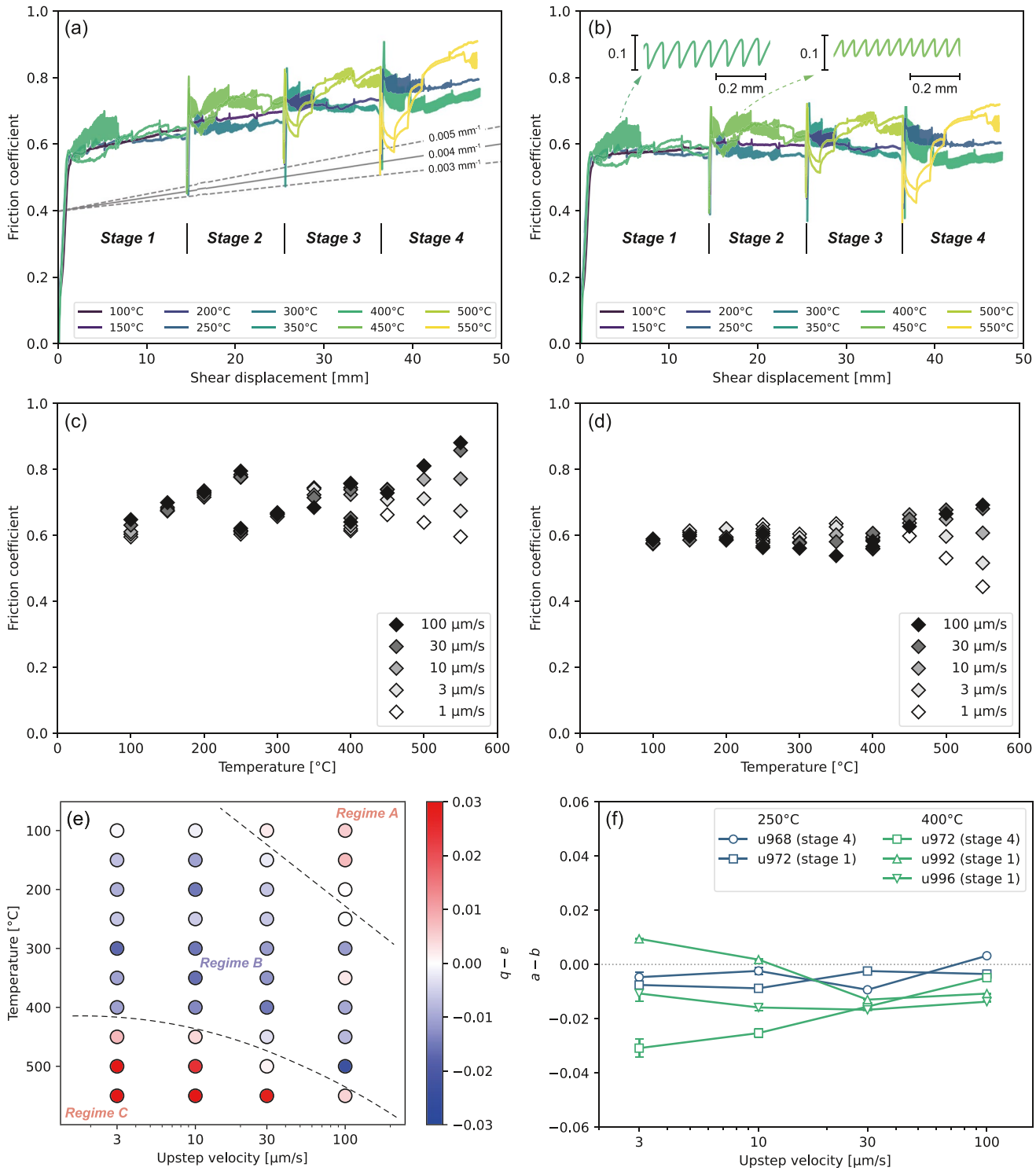

Figure 4. (a) Frictional behavior of altered basalt at $T = 100$–250°C (u968), 250–400°C (u972), and 400–550°C (u992, u996) with $\sigma_n^{eff} = P_f = 100$ MPa. Trends of μ are also indicated. (b) Frictional behavior after detrending a universal trend of 0.004 mm^{-1}. Insets show two examples of stick slip behavior at $T = 400$ and 450°C. (c) Variation in μ-values (original data) at each V-T condition. (d) Variation in μ values (detrended data) at each V-T condition. The 95% confidential intervals (CI) of these μ values are smaller than the size of markers. (e) Obtained ($a-b$) values at each V-T condition. Regime A: V-strengthening regime at high-V and low-T conditions; Regime B: V-weakening regime at wide ranging V-T conditions; Regime C: V-strengthening regime at low-V and high-T conditions. (f) Observed ($a-b$) values at 250°C and at 400°C for different shear displacements. Error bars represent the 95% CI for ($a-b$) values. See Table 1 for the displacements corresponding to the respective stages.

data may include an error in μ of ± 0.05 at most, resulting from using the bounds of 0.003 or 0.005 mm^{-1} for the slip-hardening trend (Figure 4a). Throughout, we assume that all detrended data can be treated as friction values of the tested material under a given condition, following the standard practice adopted in friction studies (Blanpied et al., 1995; Lockner et al., 1986).

The V dependence of μ was determined using quasi-instantaneous V-steps and quantified using the following equation:

$$a - b = \frac{\Delta \mu_{ss}}{\Delta \ln V}. \quad (1)$$

Here $\Delta\mu_{ss}$ is the difference between detrended μ values measured at V-conditions before and after the V-step, $\Delta \ln V$ is the difference in V measured in the logarithmic scale, and $(a-b)$ is the dimensionless value representing the V-dependence of μ as originally formulated in the rate- and state-dependent friction law (hereafter RSF law) (Dieterich, 1979; Ruina, 1983):

$$\mu = \mu_0 + a \ln\left(\frac{V}{V_0}\right) + b \ln\left(\frac{V_0 \theta}{d_c}\right), \quad (2)$$

where μ_0 is the detrended friction coefficient before a V-step, that is, at $V = V_0$, d_c is a characteristic slip displacement, and θ is a state variable. We only focus on $(a-b)$ because this parameter controls whether a fault has the potential to slip unstably or not: a fault cannot slip unstably by itself when $(a-b)$ is positive (V-strengthening) whereas a fault has the potential to nucleate an earthquake when $(a-b)$ is negative (V-weakening). Note that the value of $\Delta\mu_{ss}$ associated with a given V-step was obtained by comparing the μ value just before the V-step (μ_0) with that just after the V-step (μ_1) as follows (Figures 3e and 3f). In all experiments, fluctuations in friction data, and fluctuations in higher and lower bounds of friction values during stick slips, were generally minor or absent in the 0.3–0.7 mm displacement interval (d_{after}) following individual V-step at d_{step}. Therefore, this interval was chosen to evaluate the $(a-b)$, along with the final 0.4 mm of friction data obtained before d_{step} (this shear displacement interval is referred to as d_{before}). We obtained a local linear trend of the universally detrended μ data over d_{after}, and the μ_1 was defined by the μ value at d_{step} on the local linear trend. The μ_0 was defined by the μ at d_{step} on the local trend over d_{before}. The $\Delta\mu_{ss}$ is then obtained by $(\mu_1 - \mu_0)$. The errors of μ_0, μ_1, and $\Delta\mu_{ss}$ were estimated by 95% confidential interval arising from the local trends. The μ_0 is also used for the representative friction coefficient for each velocity-temperature-pore pressure-effective normal stress condition (Figures 4c and 4d).

2.4. Microstructural Analysis

Two constant velocity experiments (u980 and u981) and one experiment (u975) with only a single velocity step were conducted to yield samples for microstructural analysis (microstructural characterization experiments). Following testing and combined cooling and depressurization of the apparatus (duration at most 125 hr for the longest experiment u975), these samples were retrieved from the apparatus, dried for 24 hr at 50°C and impregnated with epoxy resin. Thin sections were prepared from the impregnated sample by cutting parallel to the shear direction (Figure 3c). Polarized optical microscopy and Scanning Electron microscopy (SEM, Zeiss Evo 15 located at the Electron Microscope center at Utrecht University) were used to observe the microstructure. SEM imaging was conducted using backscattered electron (BSE) mode while Energy Dispersive Spectrometry (EDS) was employed for the acquisition of chemical information.

3. Results

3.1. Mechanical Data

3.1.1. Effects of Temperature, Velocity, and Shear Displacement

The evolution of friction coefficient (μ) with displacement (d) at different temperature (T) and velocity (V) conditions, and at an effective normal stress (σ_n^{eff}) = pore pressure (P_f) = 100 MPa, is shown in Figure 4a and the detrended result is shown in Figure 4b. The relationship between detrended μ, T and V is summarized in Figure 4d, which will be used for the discussion in this study. Although the slip-hardening trend may also be influenced by pressure and velocity conditions (Den Hartog, Peach, et al., 2012; Phillips et al., 2020), we ignored them in this study, which requires further experimental considerations. The representative μ value at each P-T-V

condition was determined at the last part of each condition after detrending the universal slip-hardening trend: $\mu = \sim 0.6$ at $T < 400$°C with $V = 1$–100 μm/s; μ at low V conditions decreases with T at $T > 400$°C; μ becomes 0.45 for $V = 1$ μm/s and 0.7 for $V = 100$ μm/s at $T = 550$°C (Figure 4d).

The $(a-b)$ values vary depending on V and T. For example, at $T = 100$°C, negative $(a-b)$ values were observed at $V < 10$ μm/s, whereas positive $(a-b)$ values were observed at $V > 30$ μm/s. At $V = 100$ μm/s, positive $(a-b)$ values were observed up to $T = 200$°C, negative $(a-b)$ values up to $T = 500$°C, and positive $(a-b)$ values were again observed at higher T (Figure 4e). In general, $(a-b)$ values were positive at high-V-low-T and low-V-high-T conditions, whereas $(a-b)$ values were negative at intermediate-V-intermediate-T conditions. We define three Regimes based on the sign of $(a-b)$ values in the V-T space as follows: Regime A is the high-V-low-T range where $(a-b)$ values are positive; Regime B is the intermediate-V-intermediate-T range where $(a-b)$ values are negative; Regime C is the low-V-high-T range where $(a-b)$ values are positive (Figure 4e). Both transitions between Regimes at lower T occurred at lower V conditions, for example, the transition between Regime B and C was at $T = 400$–450°C for $V = 3$–10 μm/s whereas $T = 500$–550°C for $V = 30$–100 μm/s. Results obtained at $T = 250$ and 400°C, and at different d (Figure 4f), suggest that d has little or no systematic influence on $(a-b)$ values at 250°C, despite the slip hardening and T strengthening observed in Figures 4a–4d. Some influence of d may be present in the case of $T = 400$°C (Figure 4f), although we consider it not significant. We note that a previous study on similar altered basalt showed similar values for μ (range 0.60–0.69) and for $(a-b)$ (range −0.003 to −0.006) at a T of 150°C and V of 0.2–2 μm/s (Phillips et al., 2020), lending support to our results and detrending strategy.

3.1.2. Effects of High Pore Pressure and Low Effective Normal Stress at 200°C and 500°C

At temperature $(T) = 200$°C, the $(a-b)$ values are generally insensitive to effective normal stress (σ_n^{eff}) and to pore pressure (P_f) (Figures 5a and 5b). At $T = 500$°C $(a-b)$ has a tendency to increase with P_f (Figure 5c). The $(a-b)$ values increase with σ_n^{eff} as well but only at low V conditions (Figure 5d). Note that only positive values for $(a-b)$ were observed at high P_f (150 and 200 MPa), whereas negative $(a-b)$ values were still observed for all other P_f and σ_n^{eff} conditions.

3.1.3. Results of Low Velocity and Vacuum Dry Runs

Detrended friction coefficient (μ) values obtained for u1017, which was conducted at low velocities (V) of 0.003–1 μm/s and at a temperature (T) of 400°C, ranged from 0.52 to 0.64, similar to those in other experiments (u972, u992, u996) at 400°C (Figure 6a). The $(a-b)$ values were basically negative at all tested V conditions except for the V-step from 0.3 to 1 μm/s in u1017 and from 1 to 3 and 3–10 μm/s in u992 (Figure 6b).

Under vacuum dry conditions at $T = 100$–200°C (u1003), the detrended μ values ranged from 0.59 to 0.67 and the $(a-b)$ values were close to zero at all V-T conditions. By contrast, wet experiments at the same T and effective normal stress (σ_n^{eff}) conditions (u968) showed slightly lower μ values of 0.57–0.62, and lower $(a-b)$ values especially at lower V ($\leq$30 μm/s) and/or higher T conditions (Figures 6c–6f).

3.1.4. Microstructural Characterization Experiments: Mechanical Data Obtained in Regimes A, B, and C

The temperature (T) and velocity (V) conditions of the microstructural characterization experiments were selected on the basis of the three observed Regimes of V dependence of friction (Figure 7a). The test performed in Regime A (u981, $T = 100$°C, $V = 100$ μm/s) showed stable frictional behavior whereas stick slip behavior was observed in the test conducted in Regime B (u980, $T = 400$°C, $V = 1$ μm/s). The V-step from 1 to 0.01 μm/s in the test done in Regime C (u975, $T = 550$°C, $V = 1$ and 0.01 μm/s) showed marked V-strengthening behavior characterized by a gradual decrease to the steady state friction coefficient for $V = 0.01$ μm/s, which was about 0.3 at the shear displacement of 8.7 mm (Figure 7b).

3.2. Microstructures

The samples retrieved from the above experiments were analyzed to observe the microstructural characteristics of the three Regimes (Figure 7a): Regime A with velocity (V) strengthening at low-temperature (T)-high-V conditions; Regime B with V weakening at intermediate-T-intermediate-V conditions; and Regime C with V strengthening at high-T-low-V conditions. In Regime A, the microstructure is characterized by a wide, boundary-parallel cataclastic shear band of ~300–400 μm width, and Riedel shears, identified by open fractures (Figure 7c). The shear band is porous and the long axis of larger fragmented grains of both albite and clinopyroxene with grain

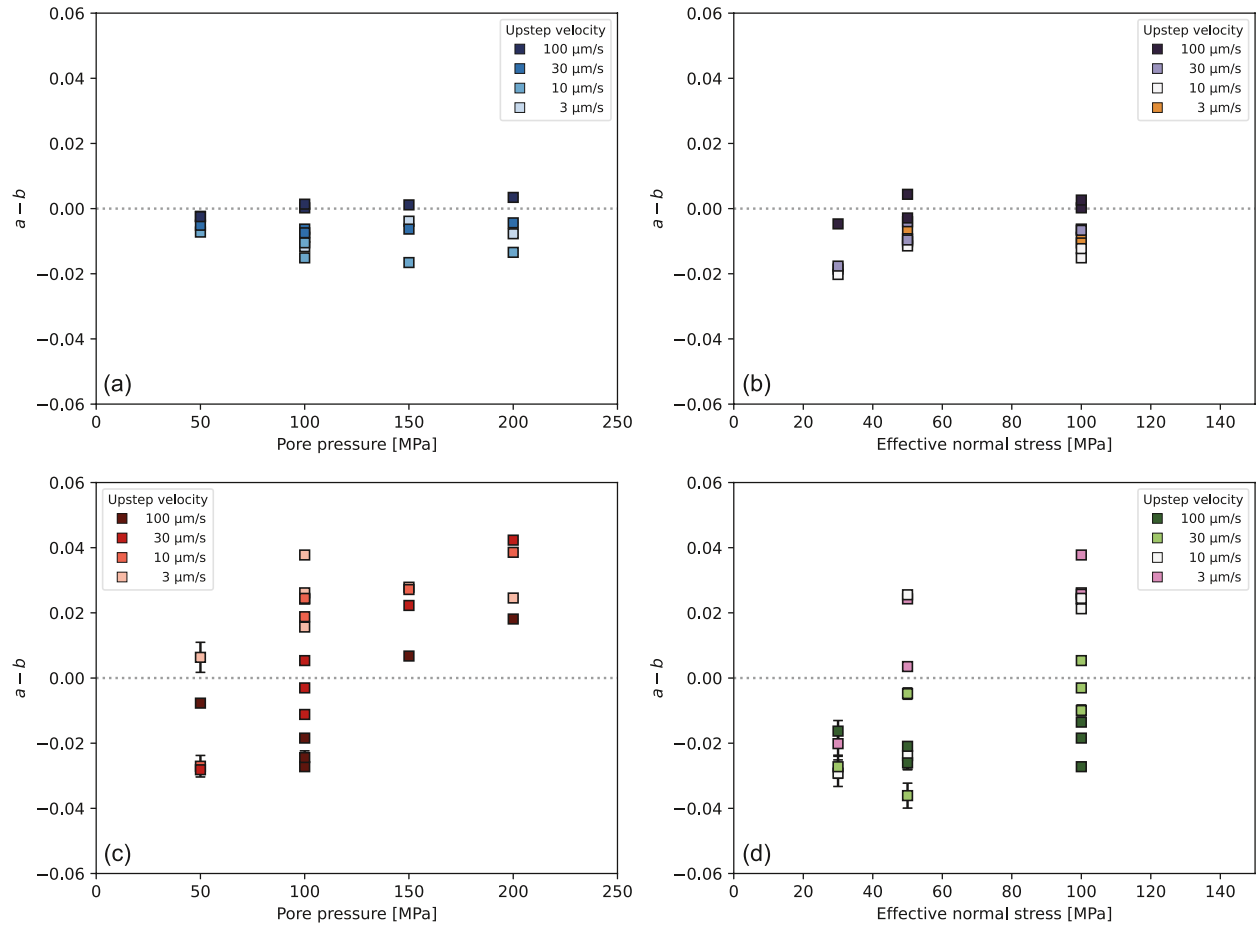

Figure 5. The $(a-b)$ values for (a) variable P_f conditions with a constant σ_n^{eff} of 100 MPa at $T = 200$°C, (b) variable σ_n^{eff} conditions with a constant P_f of 100 MPa at $T = 200$°C, (c) variable P_f conditions with a constant σ_n^{eff} of 100 MPa at $T = 500$°C, and (d) variable σ_n^{eff} conditions with a constant P_f of 100 MPa at $T = 500$°C. Error bars represent the 95% confidential intervals of $(a-b)$.

size less than ~30 μm are aligned parallel to the shear direction. Outside the shear band (center part of the gouge), grains are slightly rounded but their sizes are larger (but less than ~50 μm) than those in the shear band.

In Regime B, the shear band is narrower (~100 μm) with having a denser shear zone, namely principal slip zone (PSZ), at the center of the shear band (Figure 7d). The shear band in Regime B is denser than the shear band in Regime A. Grain size in the PSZ is reduced to sizes <1 μm. At the outside of PSZ but in the shear band, both Riedel shears, characterized by open fractures, and P foliations, characterized by aligned grains which are cataclastically fragmented (grain size ~1–10 μm), are observed. The long axis of an assemblage of fragmented grains of albite and clinopyroxene are aligned along the P foliation (Figure 8a) but the textures of these grains vary with mineralogy. At the same grain size of around 1 μm, albite grains are round and interlocking together whereas clinopyroxene grains are angular and do not show interlocking features but form porous aggregates (Figures 8b and 8c). At the area far from the shear band, grains are angular and their sizes are larger (but less than 100 μm) than those in the shear band.

In Regime C, the shear band is much narrower (~50 μm in width) and denser than that in Regime B (Figure 7e). Albite grains in the shear band are tightly interlocked and individual grains are difficult to distinguish. Grain size of clinopyroxene is less than 5 μm in the shear band (Figure 8d). At the outside of the boundary shear band, grains are angular, and their sizes are ~100 μm. Variations in textures with mineralogy are also found in Regime C where isolated pores are observed between tightly interlocking albite grains (Figures 8e and 8f), whereas clinopyroxene grains are angular and occasionally show an indentation into an albite grain at the same scale (Figure 8e). These features suggest that the albite likely underwent dissolution and precipitation processes, such as a pressure solution, whereas clinopyroxene deformed in a mostly brittle manner. Similarly, we observed that

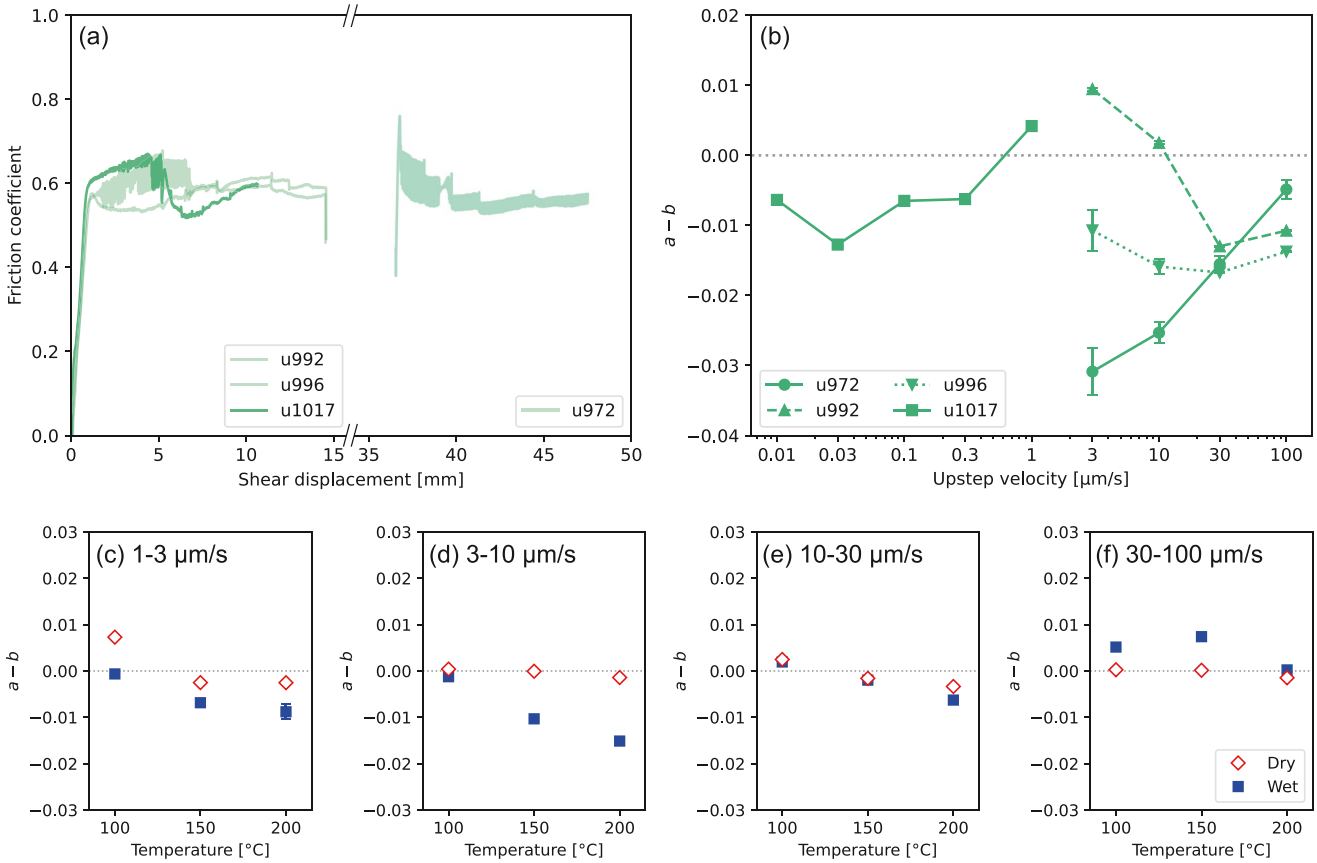

Figure 6. Results of (a) detrended μ and (b) $(a-b)$ for u1017 tested wet at low V conditions at $T = 400$°C. Also plotted are data obtained from other wet experiments performed at $T = 400$°C with $V = 1$–100 μm/s. (c–f) Results of vacuum dry experiments from $T = 100$°C–200°C (red open symbols annotated with "dry"). Blue filled symbols represent data obtained in u968 under 100 MPa P_f (annotated with "wet"). Error bars represent 95% confidential intervals of $(a-b)$ values.

large albite grains outside of the shear band tend to have pores inside characterized by unclear grain boundaries (Figure 8f). We also observed limited volumes of very thin (<1 mm) chlorite foliation between grains, subparallel to shear deformation (Figure 8f).

Results of EDS analysis (Figure 9) performed on intact and deformed samples showed no significant differences in the chemical composition of either clinopyroxene (Figure 9e) or albite (Figure 9f) between intact samples and samples deformed at different T and V conditions. As discussed in Section 4.1, although clinopyroxene decomposes into epidote and quartz at $T > 300$°C under natural conditions and on natural timescales (Kameda et al., 2017), the mineral transformation from clinopyroxene into epidote and quartz did not happen to any detectable extent during the duration of our experiments, even at $T = 550$°C (u975). Therefore, the mechanical results obtained in this study can be taken to represent the frictional behavior of the albite-clinopyroxene-chlorite assemblage at all T conditions investigated, even when the clinopyroxene is thermodynamically unstable.

4. Discussion

4.1. Deformation Micromechanisms

In our experiments, we have observed three Regimes of velocity (V) dependence of friction: (Regime A) V-strengthening at higher V and/or lower temperature (T) conditions, characterized by a thick cataclastic and porous shear band at the boundary; (Regime B) V-weakening at intermediate V-T conditions which showed a narrow, relatively dense shear band at the boundary and interlocking clusters of round albite grains along the P foliations; and (Regime C) marked V-strengthening at lower V and/or higher T conditions ($(a-b) > 0.01$ at $T > 450$°C) with a dense shear band microstructure featuring limited volume of chlorite foliations and deformation

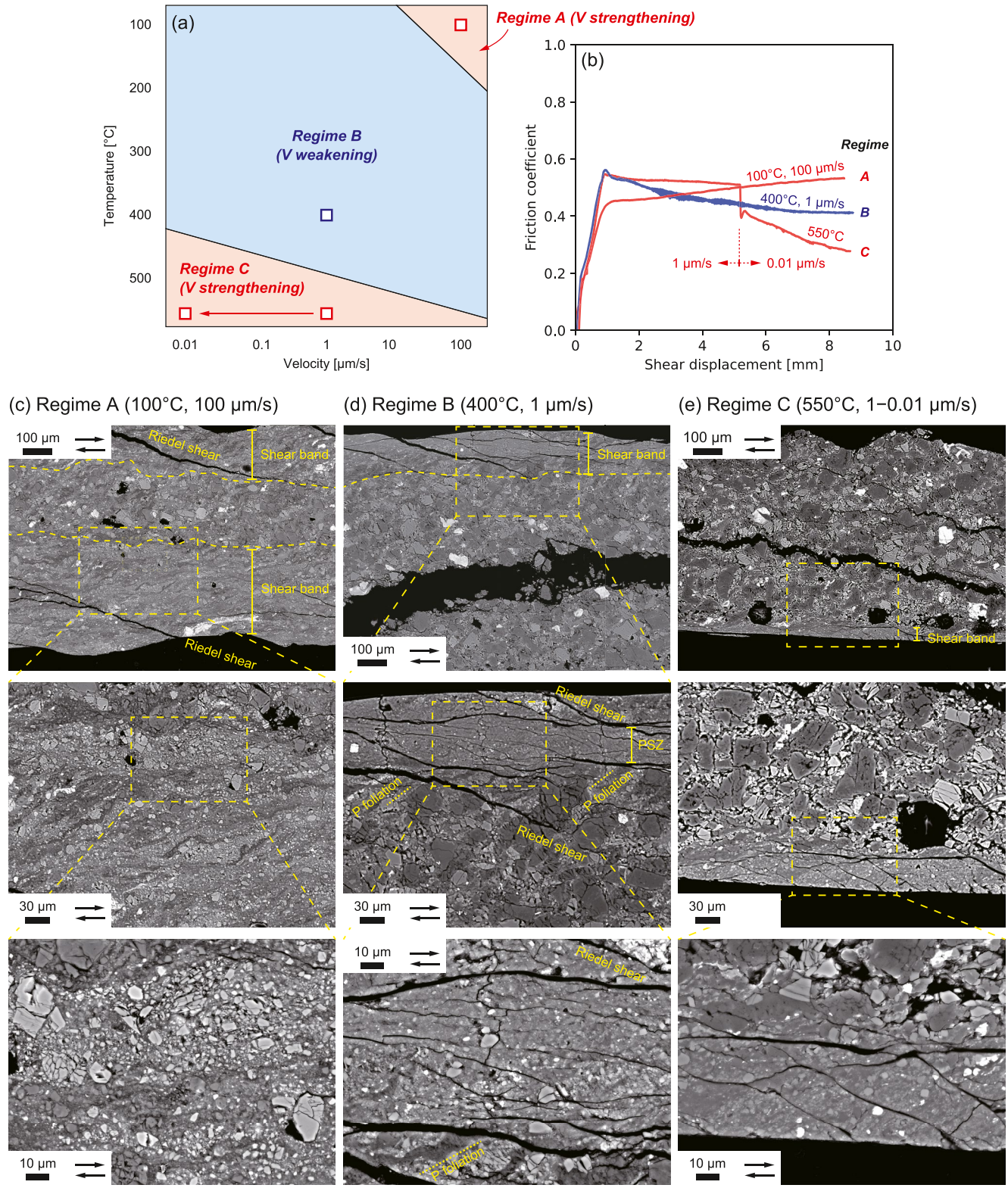

Figure 7. (a) Schematic diagram of three Regimes in *V-T* space based on Figure 4d. Experimental conditions for three microstructural characterization experiments are plotted by square markers. (b) Detrended μ values of three tests for microstructural observation. (c–e) Characteristic microstructures observed in microstructural characterization experiment in each Regime. The yellow square in each figure is the location of the image in the lower row. PSZ: principal slip zone.

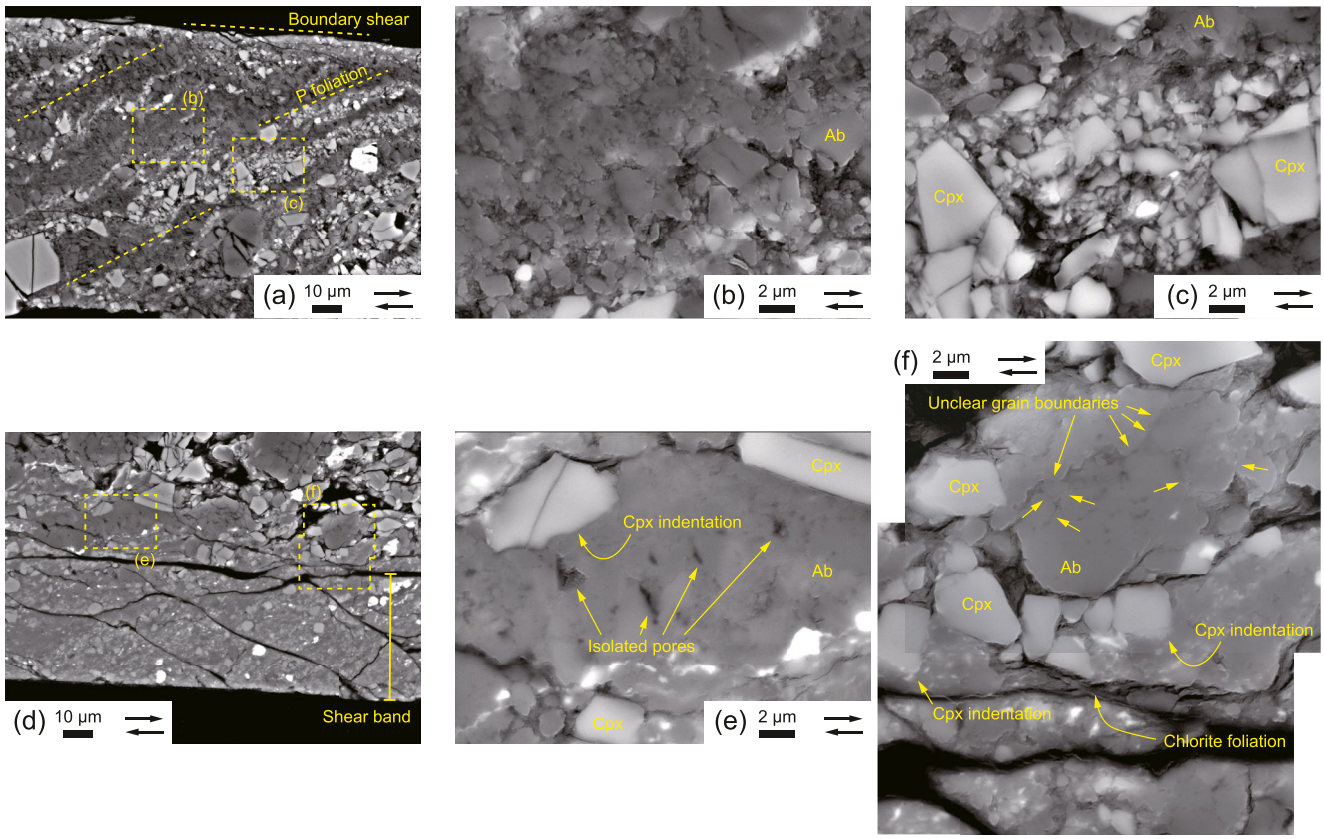

Figure 8. Characteristic microstructures for samples deformed in Regime B (a–c) and Regime C (d–f). The yellow squares in (a) and (d) are the locations of (b, c, e, f). Ab: albite; Cpx: clinopyroxene.

by dissolution and precipitation processes, possibly pressure-solution creep, in albite grains rather than clinopyroxene grains (Figures 7 and 8).

When the system is dry, fluid-assisted processes like pressure-solution creep cannot be active. We observed little dependences of ($a-b$) on V-T conditions in the case of dry experiments (conducted at V = 1–100 μm/s, T = 100–200°C, u1003, open symbols in Figures 6c–6f), in contrast to the wet experiments which showed that the transition between Regime A (V-strengthening) and B (V-weakening) occurs around V = 30–100 μm/s at T = 100–200°C (Figure 6). This difference between dry and wet experiments demonstrates that the presence of a fluid (pressure) has a large effect on the V dependence of friction even at low T conditions. As the shear band microstructures observed in Regime B and C under wet conditions are characterized by interlocking albite grains, and as the fractures in albite grains outside the shear band in Regime C also showed interlocking features (Figure 8), pressure-solution creep (Rutter & Mainprice, 1979; Spiers et al., 2004) of albite may be a possible process involved in controlling mechanical behavior.

Results from previous studies on simulated gouges prepared from halite-phyllosilicate mixtures, calcite, illite-rich shale, granite, quartz, and gabbro, under hydrothermal conditions, showed similar transitions in frictional behavior from V strengthening, V weakening, to V strengthening with respect to V or T conditions (Blanpied et al., 1995; Chen et al., 2020; Chester & Higgs, 1992; Den Hartog & Spiers, 2013; He et al., 2007; Niemeijer & Spiers, 2007; Verberne et al., 2015). This three-regime behavior can be explained by a microphysical model based on a competition between a rate/time-dependent, thermally activated deformation/compaction mechanism, such as pressure solution, and slip-dependent dilatation resulting from intergranular sliding (granular flow) characterized by mild V-strengthening, namely the Chen-Niemeijer-Spiers (CNS) model (Chen & Spiers, 2016; Niemeijer & Spiers, 2007). Strictly speaking, a V dependence of ($a-b$) undermines (is inconsistent with) the assumptions of the RSF formulation, but it supports the predictions of the microphysically-based CNS model (Chen et al., 2017; Van den Ende et al., 2018).

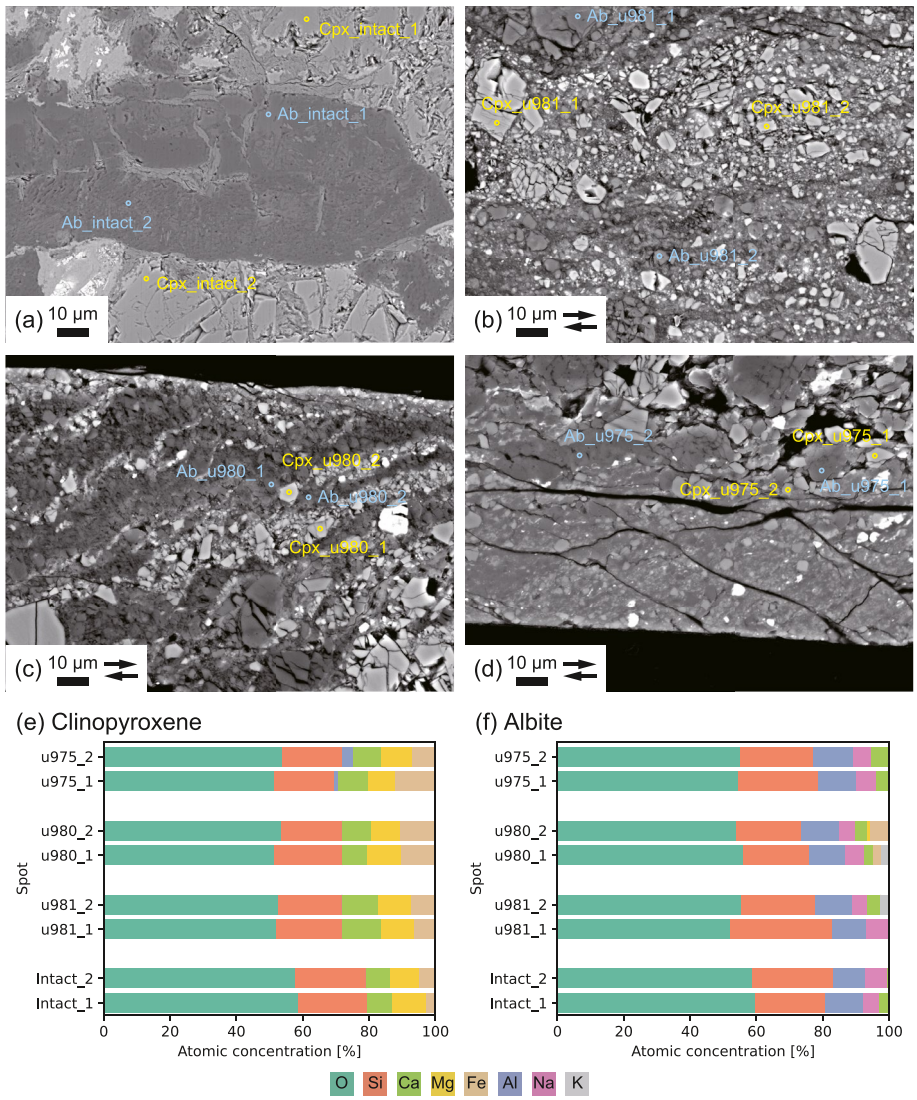

Figure 9. Results of EDS analyses on (a) intact sample, (b) sample u981 sheared at 100 μm/s and 100°C, (c) sample u980 sheared at 1 μm/s and 400°C, and (d) sample u975 sheared at 1 and 0.01 μm/s at 550°C. (e and f) Atomic concentrations of the elements shown in clinopyroxene and albite grains at the spots shown in (a) to (d). Ab: albite; Cpx: clinopyroxene.

In such a microphysical model, when V is sufficiently low or T is sufficiently high, compaction by creep of grains occurs efficiently and porosity within the gouge is kept low. Then the shearing behavior is viscous and shows significant V-strengthening behavior (Bos & Spiers, 2002; Niemeijer & Spiers, 2005, 2007). At even lower V and/or higher T, the shear strength and apparent friction coefficient μ will be controlled by non-dilatant frictional sliding on any phyllosilicate foliation (Niemeijer & Spiers, 2005). When the shear strain rate becomes fast enough for one grain to start to override the next grain, the porosity of the gouge starts to increase and the shear strength originating from dilatant frictional sliding (granular flow) decreases. This situation involves competition between the rate of dilatation due to granular flow and compaction by pressure solution, leading to a balance at steady state that is characterized by a steady state porosity and negative ($a-b$) value (Niemeijer & Spiers, 2007). When V is high or T is low enough to render compaction creep unable to compete with dilatation due to granular flow, then critical state granular flow ensues at a fixed (critical state) porosity (Niemeijer & Spiers, 2007). At this point, V-strengthening intergranular friction causes re-emergence of V-strengthening behavior at the sample scale (Chen & Spiers, 2016).

In the presently obtained microstructures, grains in the shear band formed in the test conducted in Regime A did not show interlocking features of grains but cataclastically fragmented grains were observed. By contrast, we

observed interlocking features of albite grains in both Regimes B and C (Figure 7). Significant V strengthening in Regime C also suggests a viscous deformation as the dominant deformation mechanism at the corresponding V-T conditions. Our interpretation is that pressure-solution creep of albite accommodates the ductile-compaction behavior and clinopyroxene (and albite as well in Regime A) accommodates the brittle-dilatant (granular flow) behavior, with competition between these behaviors leading to the three-Regime behavior. The model for the regime transitions predicts higher shear band porosity in Regime A and lower porosity in Regimes B and C, which is also clearly seen in our microstructural observations (Figure 7). The correspondence of the trends seen in our mechanical data and microstructures with the trends predicted by the above microphysical model implies that a model such as the CNS model can be used to justify extrapolation of the fault slip behavior seen within the altered basalt beyond the laboratory conditions explored. According to previous studies that reported on mineral compositions of basaltic zones found in different mélanges in the Shimanto accretionary complexes, albite-clinopyroxene-chlorite assemblages disappear at $T > 300$°C (Kameda et al., 2017). Therefore, our experimental results and extrapolation supported by the microphysical model can only be applied to subduction depth ranges where $T < 300$°C. At greater depths, clinopyroxene will disappear and epidote-quartz or actinolite(-quartz) will emerge, completely changing the mineral assemblage. As we did not observe any mineralogical changes in our high T experiments, either via microstructural or EDS analyses (see Section 3.2), we believe that our high T experiments can be used to understand the deformation processes that govern the frictional behavior of albite-clinopyroxene-chlorite assemblage. However, the frictional behavior obtained at $T > 300$°C does not represent the frictional behavior of altered oceanic crust at depths where these high temperatures prevail. In the discussions below, we accordingly focus on the frictional properties of subducting oceanic crust at subduction zone depths where $T < 300$°C.

4.2. Effect of Basalt Alteration on Frictional and Strength Profiles for Subducting Oceanic Crust

The above microphysical model concept for frictional behavior predicts velocity (V)-weakening behavior when pressure-solution creep of albite and dilatant/frictional granular flow occur at comparable rates. Both albite and chlorite are originally present in our uncrushed material (Figure 2), which means that those minerals are not formed during our experiments—they result from early seafloor alteration processes and subsequent subduction (Braden & Behr, 2021; Ikari et al., 2020; Kameda et al., 2011, 2017; Moore et al., 2007; Phillips et al., 2020; Ujiie et al., 2007). As seen in Figure 2, albitization produces fine albite grains from single anorthite grains and mechanically weak chlorite as well (Ramseyer et al., 1992; Rosenbauer et al., 1988). The low friction coefficient (μ) of chlorite (range 0.24–0.36) reduces the bulk strength of gouge if sufficient chlorite is present (Logan & Rauenzahn, 1987; Okamoto et al., 2019, 2020), so that altered subducting oceanic crust will be weaker than fresh oceanic basalt. In addition, finer albite grains will deform more easily via pressure solution than large grains, promoting viscous compaction and shear creep leading to V weakening (Regime B) at lower temperature (T) conditions than in fresh oceanic basalt. This effect can be expected when grain size is extensively reduced by grain comminution under natural or experimental conditions. Compared to fresh oceanic basalt (Zhang et al., 2017), the present altered basalt showed slightly lower μ (Figure 10a) and potentially unstable frictional behavior (Regime B) at $T > 100$°C, thus including temperatures expected at seismogenic zone depths (Figure 11a). Our finding of a potential for frictional instability over a wide T range also differs from findings for chlorite (Okamoto et al., 2019) and for single mineral phases of pyroxene and plagioclase (He et al., 2013). This suggests that the presence of small grains of albite as an alteration product promotes the V-weakening behavior of altered basalt under conditions that are relevant for nucleating megathrust earthquakes in subduction zones.

While the mineral compositions of basalts in the Shimanto complex are similar (Kameda et al., 2017), subducting oceanic crust will in general be characterized by varying ratios of minerals reflecting different initial compositions. For instance, if basalt originates from pillow lava containing much glassy phase, the content of saponite or chlorite will be higher upon alteration. Such a material will show a lower friction coefficient and more stable frictional sliding because of the presence of chlorite. In addition, saponite dehydration may not be complete up to 300°C in some cases (Kameda et al., 2017). Although variations in pore pressure do not affect friction parameter values in the case of our material, saponite dehydration provides fluid (Kameda et al., 2011) and, therefore, can induce pore pressure increase, if fluid drainage is slow, and subsequent reduction in shear strength. Therefore, the initial mineral composition of subducting oceanic basalt and the degree of alteration that it has undergone may change frictional behavior significantly.

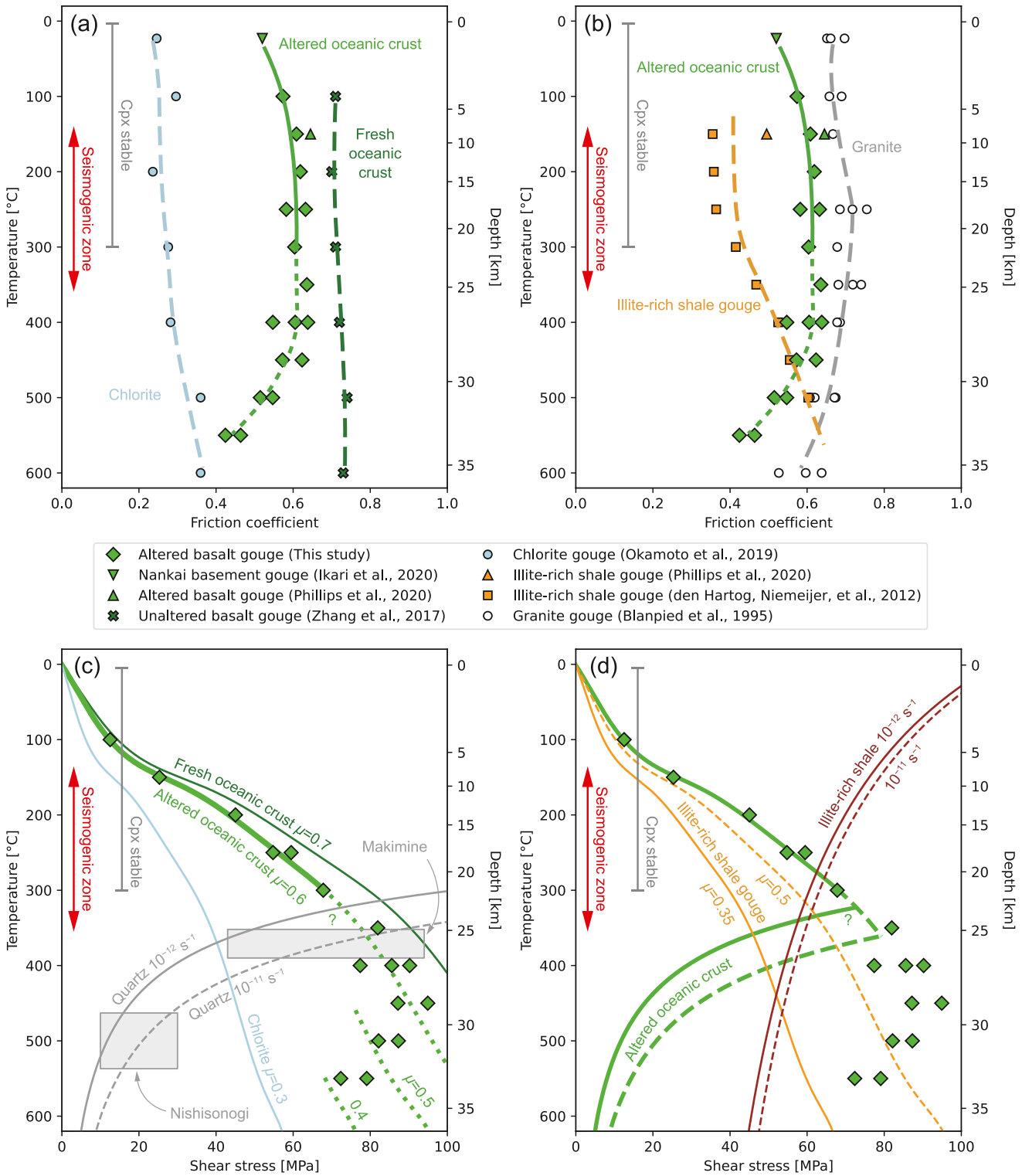

Figure 10.

Although our experimental data cannot be directly applied to depth ranges where $T > 300$°C, previous geological studies have estimated the strength of altered oceanic crust at such depths. In the Makimine mélange and Nishisonogi metamorphic rocks, SW Japan, deformed oceanic crust materials are exposed that have experienced T of 370°C and 500°C, respectively (Tulley et al., 2020). The estimated shear stresses from dynamically recrystallized

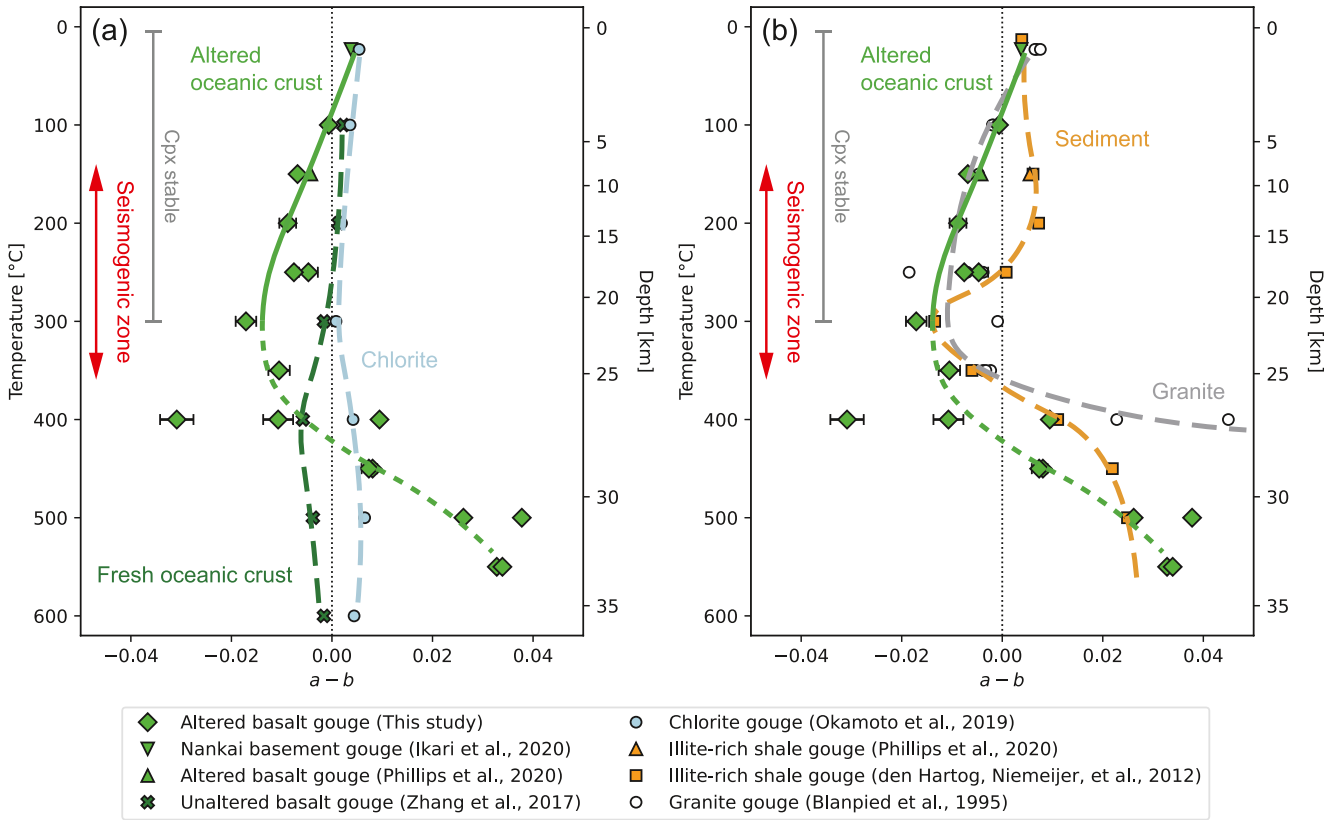

Figure 11. Depth profile of ($a-b$) values for altered oceanic crust at the V-step from V = 1–3 μm/s compared (a) with altered oceanic crust (Ikari et al., 2020; Phillips et al., 2020), fresh oceanic crust (Zhang et al., 2017), and chlorite gouge (Okamoto et al., 2019); (b) with illite-rich shale (Den Hartog, Niemeijer, et al., 2012; Phillips et al., 2020) and granite gouge (Blanpied et al., 1995). T-depth relation is from Yoshioka et al. (2013). Clinopyroxene breaks down at temperature >300°C where the curve for altered oceanic crust is shown by a dotted line; therefore, our experimental data are applicable to the temperature conditions below 300°C. Error bars represent the 95% confidential intervals of ($a-b$) values.

grain size in quartz veins are 43–94 MPa in the Makimine mélange and 10–30 MPa in the Nishisonogi metamorphic rocks, regarding these as the ductile shear strength of the subducting oceanic crust at depth (Tulley et al., 2020). An over-pressured condition with respect to the hydrostatic pore fluid pressure head in subducting oceanic crust may be expected due to a combination of dehydration of saponite around 150°C and low permeability of overlying sediment that hampers fluid escape from the oceanic crust (Kameda et al., 2011), although pervasive fluid over-pressured conditions in both sediment and oceanic crust would be also possible due to compaction. Assuming the pore pressure ratio λ (pore pressure/lithostatic pressure) = 0.8 (Tulley et al., 2020), the altered oceanic crust have 70–90 MPa of shear stress at the depth of T = 300–400°C based on the intersection of Coulomb stress of altered oceanic crust with μ = 0.6 and the ductile shear strength of quartz (Figure 10c). Therefore, we expect the depth profile of shear stress of subducting oceanic crust will follow the green line in Figure 10d. However, as we already noted, albite-clinopyroxene-chlorite assemblage used in this study is not thermodynamically stable and, frictional behavior of albite-epidote-quartz-chlorite or albite-actinolite(-quartz)-chlorite assemblages must take over as governing the strength of subducting oceanic crust. It has been suggested that

Figure 10. Depth profiles of detrended μ for altered oceanic crust at V = 1 μm/s (this study) compared (a) with altered oceanic crust (Ikari et al., 2020; Phillips et al., 2020), fresh oceanic crust (Zhang et al., 2017), and chlorite gouge (Okamoto et al., 2019); (b) with illite-rich shale (Den Hartog, Niemeijer, et al., 2012; Phillips et al., 2020) and granite gouge (Blanpied et al., 1995). Clinopyroxene breaks down at temperature >300°C where the curve for altered oceanic crust is shown by a dotted line; therefore, our experimental data can be applicable to the temperature conditions below 300°C. Depth profiles of shear stress for altered oceanic crust at V = 1 μm/s (this study) compared (c) with fresh oceanic crust (Zhang et al., 2017), chlorite gouge (Okamoto et al., 2019), estimated shear stresses at the Makimine mélange and Nishisonogi metamorphic rock (Tulley et al., 2020), and quartz rheology (Hirth et al., 2001; Tulley et al., 2020); (d) with illite-rich shale gouge (Den Hartog, Niemeijer, et al., 2012; Phillips et al., 2020), and rheology for illite-rich shale (Ibanez & Kronenberg, 1993). Shear stresses were calculated based on μ and an over-pressured condition with λ (pore pressure/lithostatic pressure) = 0.8 was assumed. Vertical direction is assumed to be the lithostatic pressure which is calculated by the product of density (2650 kg/m^3), depth, and gravitational acceleration. T-depth relation is from Yoshioka et al. (2013). The 95% confidential intervals of friction coefficients (a & b) and those of shear stress (c & d) are smaller than markers.

the presence of small amounts of quartz (3%–5%) can stabilize the frictional behavior of a fault gouge mixture of plagioclase and pyroxene because of the high solubility of quartz which inhibits the growth of contacts of plagioclase and pyroxene by pressure-solution creep due to silica saturation (He et al., 2013). Therefore, further experiments with albite-epidote-quartz-chlorite or albite-actinolite(-quartz)-chlorite system are needed to understand the fault slip behavior around the brittle-ductile transition of subducting oceanic crust and its relation to the downdip limit of seismogenic zone and deep slow earthquakes (Shibazaki & Iio, 2003). According to previous experimental data on illite-rich shale, the brittle-ductile transition for sediment may take place at a greater depth than that for oceanic crust (Den Hartog, Niemeijer, et al., 2012; Ibanez & Kronenberg, 1993). A combination of ductile behavior of oceanic crust and brittle behavior of sediment may also have an influence on seismic activity seen in deeper portions of subduction zone.

4.3. Implications for Fault Slip Activity in Subduction Zones

Regarding $(a-b)$, the altered basalt showed lower (more negative) values and hence a greater potential for unstable frictional behavior at temperatures $(T) < 300$°C than sedimentary and granitic rocks, that is over a large part of the seismogenic zone depth (Figure 11b). Therefore, altered basalt may be more prone to nucleating earthquakes than sediment throughout much of the seismogenic zone. This follows from the fact that for a velocity (V) weakening fault to nucleate an earthquake as a consequence of self-accelerating slip, the elastic shear stiffness K of surrounding rocks should fall below the critical stiffness K_c, which is directly proportional to $(b-a)$ (Dieterich, 1979; Ruina, 1983):

$$K_c = \frac{(b-a)\sigma_n^{eff}}{d_c}, \tag{3}$$

where d_c is a critical slip distance in the V-step although we do not quantify it in this study. Equation 3 shows that the unstable fault slip, that is, earthquake, is more likely to occur when $(b-a)$ and/or σ_n^{eff} are large or d_c is small.

However, since illite-rich shale gouge shows lower friction coefficient (μ) (around 0.35 to 0.5) than obtained here for altered basalt at seismogenic zone depths (Den Hartog, Niemeijer, et al., 2012; Phillips et al., 2020), the sediment is the first candidate to be sheared easily during subduction (Figure 10b) and so to host seismogenesis. On the other hand, the frictional strength of the altered oceanic crust can be lowered substantially when more chlorite is present and/or when pore pressure (P_f) is high enough and the σ_n^{eff} is low. Assuming that μ for subducting sediment is 0.35–0.5 (Den Hartog, Niemeijer, et al., 2012) and 0.6 for altered oceanic crust, a higher P_f is required in the altered oceanic crust than that in the sedimentary facies to cause the frictional strength of the altered oceanic crust to be lower than that of the sedimentary facies: for example, the pore pressure ratio (λ) for the altered oceanic crust should be 0.88 to 0.83 to render the apparent frictional strengths of the sedimentary and oceanic materials the same when λ for the sediment is 0.8. Necessary pore pressure changes are 17.3 MPa to shift from $\lambda = 0.8$ to 0.88, and 6.9 MPa to shift from $\lambda = 0.8$ to 0.83 at $T = 150$°C. When the frictional strength of the altered oceanic crust is lower than that of sediment through such pore fluid over-pressuring, deformation at the plate boundary would be accommodated by altered oceanic crust rather than by the sediment, and the accumulated stress along the plate boundary would be released by earthquake nucleation within the oceanic crust at the seismogenic zone depths (~5–25 km) where we obtained V-weakening of altered basalt (Phillips et al., 2020).

It is important to note here that, both a decrease in σ_n^{eff} and/or an increase in P_f do not influence the $(a-b)$ value of altered basalt at $T = 200$°C unlike blueschist, actinolite-chlorite mixture, and other materials (Bedford et al., 2021; Okamoto et al., 2020; Okuda et al., 2021; Sawai et al., 2016). Such an over-pressured condition possibly induces a slower slip because the nucleation size L_c, defined as follows (Dieterich, 1986):

$$L_c = \frac{\xi G}{K_c} = \frac{\xi G d_c}{(b-a)\sigma_n^{eff}}, \tag{4}$$

where ξ is a geometric constant of order 1 and G is the shear modulus of surrounding rock, becomes large. Therefore, significantly over-pressured oceanic crust may host slip at a low slip rate, although the effects of σ_n^{eff} and P_f on d_c are unknown. Since sedimentary facies at shallow depths (<10 km) along the décollement are over-pressured due to sediment compaction (Saffer et al., 2008; Tsuji et al., 2014), coseismic rupture may propagate within the weak sedimentary facies rather than the altered oceanic crust at a depth of <10 km. Such

situations might lead rupture on the décollement to "stepup" from a nucleation phase in the oceanic crust within the seismogenic zone (~5–25 km) to a rupture propagation phase in the sedimentary facies at shallower depths which will result in the observation of décollement stepdown. In addition, further experimental studies on sediments may be needed to more fully understand the difference in frictional behavior between sediments and altered oceanic crust because detrital materials also often contain anorthite that can be altered into albite at the same T condition in shallow depths of subduction zones.

5. Conclusion

Seismological and geological studies suggest that the plate boundary fault (décollement) in subduction zones possibly develops within the subducting oceanic crust rather than sedimentary facies in the seismogenic zone depths. To understand the frictional properties of the subducting oceanic crust, we performed hydrothermal friction experiments on altered basalt at temperatures (T) of 100–550°C, effective normal stresses (σ_n^{eff}) of 30–100 MPa, pore pressure (P_f) of 50–200 MPa, and velocity conditions (V) of 1–100 μm/s. Friction coefficient (μ) of the altered basalt was about 0.6 for all V conditions at $T < 400$°C, and became 0.45 at $T = 550$°C and $V = 1$ μm/s with V-strengthening behavior to $\mu = 0.7$ at $V = 100$ μm/s considering a slip hardening trend of 0.004 mm^{-1}. Three regimes of V dependence were found: Regime A was at lower T (<200°C) and higher V (>30 μm/s) showing V-strengthening behavior; Regime B was at intermediate T (100–450°C) and almost all the V conditions showing V-weakening behavior; Regime C was at higher T (>500°C) and lower V showing V-strengthening behavior. These regimes can be explained by a microphysical model that considers a balance between compaction creep and dilatant frictional behavior at grain boundaries. Microstructural observations indicated that pressure-solution in albite likely controls the creep component of deformation, which shifts Regime B to higher V conditions at a given T. Alteration of oceanic crust during subduction produces fine grains of albite contributing to the viscous deformation by pressure-solution creep under natural conditions. Because albitization also produces mechanically weak chlorite, altered oceanic crust can have a similar frictional strength to the sediment, which is also affected by P_f and thus σ_n^{eff} conditions. The velocity weakening and hence potentially unstable frictional behavior of altered basalt over a wide T range suggest that megathrust earthquakes could nucleate within the oceanic crust at seismogenic zone depths.

Data Availability Statement

Experimental data are freely available from the Yoda data repository: https://public.yoda.uu.nl/geo/UU01/Q0VVEX.html.

Acknowledgments
Comments from two anonymous reviewers are greatly appreciated for improving the clarity of this study. We thank Thony van der Gon Netscher, Gerard Kuijpers, and Floris van Oort (Utrecht University) for technical supports of ring shear apparatus, Yuichi Okuma and Ippei Yamamoto (AORI, University of Tokyo) for the field work at Mugi mélange, and Huiru Lei, Eric Hellebrand, and Oliver Plümper (Utrecht University) for the SEM works. This work benefited from EPOS-NL Facility Access to Earth Simulation Lab–High Pressure and Temperature lab (ESL-HPT), supported by the Dutch Research Council (NWO), and from KAKENHI grants (JP20J20413 to H. Okuda; JP19H04621, JP21H01189, and JP21H05202 to A. Yamaguchi). H. Okuda is supported by DC1 fellowship and Overseas Challenge Program for Young Researchers from Japan Society for the Promotion of Science (JSPS).

References

Baumgartner, P. O., & Denyer, P. (2006). Evidence for middle Cretaceous accretion at Santa Elena peninsula (Santa Rosa accretionary complex), Costa Rica. *Geológica Acta*, *4*(1–2), 179–191. https://doi.org/10.1344/105.000000364

Bedford, J. D., Faulkner, D. R., Allen, M. J., & Hirose, T. (2021). The stabilizing effect of high pore-fluid pressure along subduction megathrust faults: Evidence from friction experiments on accretionary sediments from the Nankai Trough. *Earth and Planetary Science Letters*, *574*, 117161. https://doi.org/10.1016/j.epsl.2021.117161

Blanpied, M. L., Lockner, D. A., & Byerlee, J. D. (1995). Frictional slip of granite at hydrothermal conditions. *Journal of Geophysical Research*, *100*(B7), 13045–13064. https://doi.org/10.1029/95JB00862

Bos, B., & Spiers, C. J. (2002). Frictional-viscous flow of phyllosilicate-bearing fault rock: Microphysical model and implications for crustal strength profiles. *Journal of Geophysical Research*, *107*(B2), 2028. https://doi.org/10.1029/2001JB000301

Braden, Z., & Behr, W. M. (2021). Weakening mechanisms in a basalt-hosted subduction megathrust fault segment, southern Alaska. *Journal of Geophysical Research: Solid Earth*, *126*(9), e2021JB022039. https://doi.org/10.1029/2021JB022039

Buchs, D. M., Arculus, R. J., Baumgartner, P. O., Baumgartner-Mora, C., & Ulianov, A. (2010). Late Cretaceous arc development on the SW margin of the Caribbean plate: Insights from the Golfito, Costa Rica, and Azuero, Panama, complexes. *Geochemistry, Geophysics, Geosystems*, *11*(7), Q07S24. https://doi.org/10.1029/2009GC002901

Chen, J., & Spiers, C. J. (2016). Rate and state frictional and healing behavior of carbonate fault gouge explained using microphysical model. *Journal of Geophysical Research: Solid Earth*, *121*(12), 8642–8665. https://doi.org/10.1002/2016JB013470

Chen, J., Niemeijer, A. R., & Spiers, C. J. (2017). Microphysically derived expressions for rate-and-state friction parameters, a, b, and D c. *Journal of Geophysical Research: Solid Earth*, *122*(12), 9627–9657. https://doi.org/10.1002/2017JB014226

Chen, J., Verberne, B. A., & Niemeijer, A. R. (2020). Flow-to-friction transition in simulated calcite gouge: Experiments and microphysical modeling. *Journal of Geophysical Research: Solid Earth*, *125*(11), e2020JB019970. https://doi.org/10.1029/2020JB019970

Chester, F. M., & Higgs, N. G. (1992). Multimechanism friction constitutive model for ultrafine quartz gouge at hypocentral conditions. *Journal of Geophysical Research*, *97*(B2), 1859–1870. https://doi.org/10.1029/91JB02349

Chester, F. M., Rowe, C. D., Ujiie, K., Kirkpatrick, J. D., Regalla, C., Remitti, F., et al. (2013). Structure and composition of the plate-boundary slip zone for the 2011 Tohoku-Oki Earthquake. *Science*, *342*(6163), 1208–1211. https://doi.org/10.1126/science.1243719

Den Hartog, S. A. M., & Spiers, C. J. (2013). Influence of subduction zone conditions and gouge composition on frictional slip stability of megathrust faults. *Tectonophysics*, *600*, 75–90. https://doi.org/10.1016/j.tecto.2012.11.006

Den Hartog, S. A. M., Niemeijer, A. R., & Spiers, C. J. (2012b). New constraints on megathrust slip stability under subduction zone P–T conditions. *Earth and Planetary Science Letters*, *353–354*, 240–252. https://doi.org/10.1016/j.epsl.2012.08.022

Den Hartog, S. A. M., Peach, C. J., De Winter, D. A. M., Spiers, C. J., & Shimamoto, T. (2012a). Frictional properties of megathrust fault gouges at low sliding velocities: New data on effects of normal stress and temperature. *Journal of Structural Geology*, *38*, 156–171. https://doi.org/10.1016/j.jsg.2011.12.001

Dieterich, J. H. (1979). Modeling of rock friction: 1. Experimental results and constitutive equations. *Journal of Geophysical Research*, *84*(B5), 2161–2168. https://doi.org/10.1029/JB084iB05p02161

Dieterich, J. H. (1986). A model for the nucleation of earthquake slip. In S. Das, J. Boatwright, & C. H. Scholz (Eds.), *Earthquake Source Mechanics*. https://doi.org/10.1029/GM037p0037

Fagereng, Å., & Cooper, A. F. (2010). Petrology of metabasalts from the Chrystalls Beach accretionary mélange – Implications for tectonic setting and terrane origin. *New Zealand Journal of Geology and Geophysics*, *53*(1), 57–70. https://doi.org/10.1080/00288301003631806

Hara, H., & Kimura, K. (2008). Metamorphic and cooling history of the shimanto accretionary complex, Kyushu, Southwest Japan: Implications for the timing of out-of-sequence thrusting. *Island Arc*, *17*(4), 546–559. https://doi.org/10.1111/j.1440-1738.2008.00636.x

He, C., Luo, L., Hao, Q. M., & Zhou, Y. (2013). Velocity-weakening behavior of plagioclase and pyroxene gouges and stabilizing effect of small amounts of quartz under hydrothermal conditions. *Journal of Geophysical Research: Solid Earth*, *118*(7), 3408–3430. https://doi.org/10.1002/jgrb.50280

He, C., Wang, Z., & Yao, W. (2007). Frictional sliding of gabbro gouge under hydrothermal conditions. *Tectonophysics*, *445*(3–4), 353–362. https://doi.org/10.1016/j.tecto.2007.09.008

Hirth, G., Teyssier, C., & Dunlap, J. W. (2001). An evaluation of quartzite flow laws based on comparisons between experimentally and naturally deformed rocks. *International Journal of Earth Sciences*, *90*(1), 77–87. https://doi.org/10.1007/s005310000152

Humphris, S. E., & Thompson, G. (1978). Hydrothermal alteration of oceanic basalts by seawater. *Geochimica et Cosmochimica Acta*, *42*(1), 107–125. https://doi.org/10.1016/0016-7037(78)90221-1

Hyndman, R. D., Yamano, M., & Oleskevich, D. A. (1997). The seismogenic zone of subduction thrust faults. *Island Arc*, *6*(3), 244–260. https://doi.org/10.1111/j.1440-1738.1997.tb00175.x

Ibanez, W. D., & Kronenberg, A. K. (1993). Experimental deformation of shale: Mechanical properties and microstructural indicators of mechanisms. *International Journal of Rock Mechanics and Mining Sciences & Geomechanics Abstracts*, *30*(7), 723–734. https://doi.org/10.1016/0148-9062(93)90014-5

Ikari, M. J., & Hüpers, A. (2021). Velocity-weakening friction induced by laboratory-controlled lithification. *Earth and Planetary Science Letters*, *554*, 116682. https://doi.org/10.1016/j.epsl.2020.116682

Ikari, M. J., Wilckens, F. K., & Saffer, D. M. (2020). Implications of basement rock alteration in the Nankai Trough, Japan for subduction megathrust slip behavior. *Tectonophysics*, *774*, 228275. https://doi.org/10.1016/j.tecto.2019.228275

Ikesawa, E., Kimura, G., Sato, K., Ikehara-Ohmori, K., Kitamura, Y., Yamaguchi, A., et al. (2005). Tectonic incorporation of the upper part of oceanic crust to overriding plate of a convergent margin: An example from the cretaceous–early Tertiary Mugi Mélange, the Shimanto Belt, Japan. *Tectonophysics*, *401*(3–4), 217–230. https://doi.org/10.1016/j.tecto.2005.01.005

Ikesawa, E., Sakaguchi, A., & Kimura, G. (2003). Pseudotachylyte from an ancient accretionary complex: Evidence for melt generation during seismic slip along a master décollement? *Geology*, *31*(7), 637–640. https://doi.org/10.1130/0091-7613(2003)031<0637:PFAAAC>2.0.CO;2

Kameda, J., Inoue, S., Tanikawa, W., Yamaguchi, A., Hamada, Y., Hashimoto, Y., & Kimura, G. (2017). Alteration and dehydration of subducting oceanic crust within subduction zones: Implications for décollement step-down and plate-boundary seismogenesis. *Earth Planets and Space*, *69*(1), 52. https://doi.org/10.1186/s40623-017-0635-1

Kameda, J., Yamaguchi, A., Saito, S., Sakuma, H., Kawamura, K., & Kimura, G. (2011). A new source of water in seismogenic subduction zones. *Geophysical Research Letters*, *38*(22), L22306. https://doi.org/10.1029/2011GL048883

Kawai, T., Windley, B. F., Terabayashi, M., Yamamoto, H., Maruyama, S., Omori, S., et al. (2007). Geotectonic framework of the Blueschist Unit on Anglesey-Lleyn, UK, and its role in the development of a Neoproterozoic accretionary orogen. *Precambrian Research*, *153*(1–2), 11–28. https://doi.org/10.1016/j.precamres.2006.11.002

Kimura, G., & Ludden, J. (1995). Peeling oceanic crust in subduction zones. *Geology*, *23*(3), 217–220. https://doi.org/10.1130/0091-7613(1995)023<0217:POCISZ>2.3.CO;2

Kimura, G., Yamaguchi, A., Hojo, M., Kitamura, Y., Kameda, J., Ujiie, K., et al. (2012). Tectonic mélange as fault rock of subduction plate boundary. *Tectonophysics*, *568–569*, 25–38. https://doi.org/10.1016/j.tecto.2011.08.025

Kimura, H., Takeda, T., Obara, K., & Kasahara, K. (2010). Seismic evidence for active underplating below the megathrust earthquake zone in Japan. *Science*, *329*(5988), 210–212. https://doi.org/10.1126/science.1187115

Kitamura, Y., Sato, K., Ikesawa, E., Ikehara-Ohmori, K., Kimura, G., Kondo, H., et al. (2005). Mélange and its seismogenic roof décollement: A plate boundary fault rock in the subduction zone–an example from the shimanto belt, Japan. *Tectonics*, *24*(5), TC5012. https://doi.org/10.1029/2004TC001635

Kusky, T. M., & Bradley, D. C. (1999). Kinematic analysis of mélange fabrics: Examples and applications from the McHugh complex, Kenai Peninsula, Alaska. *Journal of Structural Geology*, *21*(12), 1773–1796. https://doi.org/10.1016/S0191-8141(99)00105-4

Kusky, T. M., Windley, B. F., Safonova, I., Wakita, K., Wakabayashi, J., Polat, A., & Santosh, M. (2013). Recognition of ocean plate stratigraphy in accretionary orogens through Earth history: A record of 3.8 billion years of sea floor spreading, subduction, and accretion. *Gondwana Research*, *24*(2), 501–547. https://doi.org/10.1016/j.gr.2013.01.004

Leggett, J. K., McKerrow, W. S., & Eales, M. H. (1979). The southern uplands of Scotland: A lower palaeozoic accretionary prism. *Journal of the Geological Society*, *136*(6), 755–770. https://doi.org/10.1144/gsjgs.136.6.0755

Lockner, D. A., Summers, R., & Byerlee, J. D. (1986). Effects of temperature and sliding rate on frictional strength of granite. *Pure and Applied Geophysics*, *124*(3), 445–469. https://doi.org/10.1007/BF00877211

Logan, J. M., & Rauenzahn, K. A. (1987). Frictional dependence of gouge mixtures of quartz and montmorillonite on velocity, composition and fabric. *Tectonophysics*, *144*(1–3), 87–108. https://doi.org/10.1016/0040-1951(87)90010-2

Marone, C., & Scholz, C. H. (1989). Particle-size distribution and microstructures within simulated fault gouge. *Journal of Structural Geology*, *11*(7), 799–814. https://doi.org/10.1016/0191-8141(89)90099-0

Maruyama, S., Kawai, T., & Windley, B. F. (2010). Ocean plate stratigraphy and its imbrication in an accretionary orogen: The Mona complex, Anglesey–Lleyn, Wales, UK. *Geological Society, London, Special Publications*, *338*(1), 55–75. https://doi.org/10.1144/SP338.4

Matsumura, M., Hashimoto, Y., Kimura, G., Ohmori-Ikehara, K., Enjohji, M., & Ikesawa, E. (2003). Depth of oceanic-crust underplating in a subduction zone: Inferences from fluid-inclusion analyses of crack-seal veins. *Geology*, *31*(11), 1005–1008. https://doi.org/10.1130/G19885.1

Meneghini, F., & Moore, J. C. (2007). Deformation and hydrofracture in a subduction thrust at seismogenic depths: The Rodeo Cove thrust zone, Marin Headlands, California. *The Geological Society of America Bulletin*, *119*(1–2), 174–183. https://doi.org/10.1130/B25807.1

Miyazaki, S., & Heki, K. (2001). Crustal velocity field of southwest Japan: Subduction and arc-arc collision. *Journal of Geophysical Research*, *106*(B3), 4305–4326. https://doi.org/10.1029/2000JB900312

Moore, J. C., Rowe, C. D., & Meneghini, F. (2007). How accretionary prisms elucidate seismogenesis in subduction zones. In *The seismogenic zone of subduction thrust faults* (pp. 288–315). Columbia University Press. https://doi.org/10.7312/dixo13866-010

Mukoyoshi, H., Sakaguchi, A., Otsuki, K., Hirono, T., & Soh, W. (2006). Co-seismic frictional melting along an out-of-sequence thrust in the Shimanto accretionary complex. Implications on the tsunamigenic potential of splay faults in modern subduction zones. *Earth and Planetary Science Letters*, *245*(1–2), 330–343. https://doi.org/10.1016/j.epsl.2006.02.039

Niemeijer, A. R., & Spiers, C. J. (2005). Influence of phyllosilicates on fault strength in the brittle-ductile transition: Insights from rock analogue experiments. *Geological Society, London, Special Publications*, *245*(1), 303–327. https://doi.org/10.1144/GSL.SP.2005.245.01.15

Niemeijer, A. R., & Spiers, C. J. (2007). A microphysical model for strong velocity weakening in phyllosilicate-bearing fault gouges. *Journal of Geophysical Research*, *112*(B10), B10405. https://doi.org/10.1029/2007JB005008

Niemeijer, A. R., Boulton, C., Toy, V. G., Townend, J., & Sutherland, R. (2016). Large-displacement, hydrothermal frictional properties of DFDP-1 fault rocks, Alpine Fault, New Zealand: Implications for deep rupture propagation. *Journal of Geophysical Research: Solid Earth*, *121*(2), 624–647. https://doi.org/10.1002/2015JB012593

Okamoto, A. S., Niemeijer, A. R., Takeshita, T., Verberne, B. A., & Spiers, C. J. (2020). Frictional properties of actinolite-chlorite gouge at hydrothermal conditions. *Tectonophysics*, *779*, 228377. https://doi.org/10.1016/j.tecto.2020.228377

Okamoto, A. S., Verberne, B. A., Niemeijer, A. R., Takahashi, M., Shimizu, I., Ueda, T., & Spiers, C. J. (2019). Frictional properties of simulated chlorite gouge at hydrothermal conditions: Implications for subduction megathrusts. *Journal of Geophysical Research: Solid Earth*, *124*(5), 4545–4565. https://doi.org/10.1029/2018JB017205

Okuda, H., Katayama, I., Sakuma, H., & Kawai, K. (2021). Effect of normal stress on the frictional behavior of brucite: Application to slow earthquakes at the subduction plate interface in the mantle wedge. *Solid Earth*, *12*(1), 171–186. https://doi.org/10.5194/se-12-171-2021

Oleskevich, D. A., Hyndman, R. D., & Wang, K. (1999). The updip and downdip limits to great subduction earthquakes: Thermal and structural models of Cascadia, south Alaska, SW Japan, and Chile. *Journal of Geophysical Research*, *104*(B7), 14965–14991. https://doi.org/10.1029/1999JB900060

Onishi, C. T., Kimura, G., Hashimoto, Y., Ikehara-Ohmori, K., & Watanabe, T. (2001). Deformation history of tectonic melange and its relationship to the underplating process and relative plate motion: An example from the deeply buried Shimanto Belt, SW Japan. *Tectonics*, *20*(3), 376–393. https://doi.org/10.1029/1999TC001154

Park, J.-O., Tsuru, T., Kodaira, S., Cummins, P. R., & Kaneda, Y. (2002). Splay fault branching along the Nankai subduction zone. *Science*, *297*(5584), 1157–1160. https://doi.org/10.1126/science.1074111

Phillips, N. J., Belzer, B., French, M. E., Rowe, C. D., & Ujiie, K. (2020). Frictional strengths of subduction thrust rocks in the region of shallow slow earthquakes. *Journal of Geophysical Research: Solid Earth*, *125*(3), e2019JB018888. https://doi.org/10.1029/2019JB018888

Phillips, N. J., Rowe, C. D., & Ujiie, K. (2019). For how long are pseudotachylytes strong? Rapid alteration of basalt-hosted pseudotachylytes from a shallow subduction complex. *Earth and Planetary Science Letters*, *518*, 108–115. https://doi.org/10.1016/j.epsl.2019.04.033

Ramseyer, K., Boles, J. R., & Lichtner, P. C. (1992). Mechanism of plagioclase albitization. *Journal of Sedimentary Petrology*, *62*(3), 349–356. https://doi.org/10.1306/D42678FC-2B26-11D7-8648000102C1865D

Raymond, L. A. (2019). Perspectives on the roles of melanges in subduction accretionary complexes: A review. *Gondwana Research*, *74*, 68–89. https://doi.org/10.1016/j.gr.2019.03.005

Rosenbauer, R. J., Bischoff, J. L., & Zierenberg, R. A. (1988). The laboratory albitization of mid-ocean ridge basalt. *The Journal of Geology*, *96*(2), 237–244. https://doi.org/10.1086/629213

Ruina, A. L. (1983). Slip instability and state variable friction laws. *Journal of Geophysical Research*, *88*(B12), 10359–10370. https://doi.org/10.1029/JB088iB12p10359

Rutter, E. H., & Mainprice, D. (1979). On the possibility of slow fault slip controlled by a diffusive mass transfer process. *Gerlands Beitrage Zur Geophysik*, *88*, 154–162.

Saffer, D. M., & Marone, C. (2003). Comparison of smectite- and illite-rich gouge frictional properties: Application to the updip limit of the seismogenic zone along subduction megathrusts. *Earth and Planetary Science Letters*, *215*(1–2), 219–235. https://doi.org/10.1016/S0012-821X(03)00424-2

Saffer, D. M., Underwood, M. B., & McKiernan, A. W. (2008). Evaluation of factors controlling smectite transformation and fluid production in subduction zones: Application to the Nankai trough. *Island Arc*, *17*(2), 208–230. https://doi.org/10.1111/j.1440-1738.2008.00614.x

Sakaguchi, A., Chester, F. M., Curewitz, D., Fabbri, O., Goldsby, D. L., Kimura, G., et al. (2011). Seismic slip propagation to the updip end of plate boundary subduction interface faults: Vitrinite reflectance geothermometry on integrated ocean drilling program NanTro SEIZE cores. *Geology*, *39*(4), 395–398. https://doi.org/10.1130/G31642.1

Sawai, M., Niemeijer, A. R., Plümper, O., Hirose, T., & Spiers, C. J. (2016). Nucleation of frictional instability caused by fluid pressurization in subducted blueschist. *Geophysical Research Letters*, *43*(6), 2543–2551. https://doi.org/10.1002/2015GL067569

Scuderi, M. M., Collettini, C., Viti, C., Tinti, E., & Marone, C. (2017). Evolution of shear fabric in granular fault gouge from stable sliding to stick slip and implications for fault slip mode. *Geology*, *45*(8), 731–734. https://doi.org/10.1130/G39033.1

Seno, T., Stein, S., & Gripp, A. E. (1993). A model for the motion of the Philippine Sea plate consistent with NUVEL-1 and geological data. *Journal of Geophysical Research*, *98*(B10), 17941–17948. https://doi.org/10.1029/93JB00782

Shibazaki, B., & Iio, Y. (2003). On the physical mechanism of silent slip events along the deeper part of the seismogenic zone. *Geophysical Research Letters*, *30*(9), 1489. https://doi.org/10.1029/2003GL017047

Spiers, C. J., De Meer, S., Niemeijer, A. R., & Zhang, X. (2004). Kinetics of rock deformatino by pressure solution and the role of thin aqueous films. In S. Nakashima (Ed.), *Physicochemistry of water in geological and biological system* (pp. 129–158). University Academy Press, Inc.

Takeshita, T., Yagi, K., Gouzu, C., Hyodo, H., & Itaya, T. (2015). Extensive normal faulting during exhumation revealed by the spatial variation of phengite K-Ar ages in the Sambagawa metamorphic rocks, central Shikoku, SW Japan. *Island Arc*, *24*(2), 245–262. https://doi.org/10.1111/iar.12104

Tsuji, T., Kamei, R., & Pratt, R. G. (2014). Pore pressure distribution of a mega-splay fault system in the Nankai trough subduction zone: Insight into up-dip extent of the seismogenic zone. *Earth and Planetary Science Letters*, *396*, 165–178. https://doi.org/10.1016/j.epsl.2014.04.011

Tulley, C. J., Fagereng, Å., & Ujiie, K. (2020). Hydrous oceanic crust hosts megathrust creep at low shear stresses. *Science Advances*, *6*(22), eaba1529. https://doi.org/10.1126/sciadv.aba1529

Ujiie, K., Yamaguchi, A., Kimura, G., & Toh, S. (2007). Fluidization of granular material in a subduction thrust at seismogenic depths. *Earth and Planetary Science Letters*, *259*(3–4), 307–318. https://doi.org/10.1016/j.epsl.2007.04.049

Van den Ende, M. P. A., Chen, J., Ampuero, J.-P., & Niemeijer, A. R. (2018). A comparison between rate-and-state friction and microphysical models, based on numerical simulations of fault slip. *Tectonophysics*, *733*, 273–295. https://doi.org/10.1016/j.tecto.2017.11.040

Verberne, B. A., Niemeijer, A. R., De Bresser, J. H. P., & Spiers, C. J. (2015). Mechanical behavior and microstructure of simulated calcite fault gouge sheared at 20–600°C: Implications for natural faults in limestones. *Journal of Geophysical Research: Solid Earth*, *120*(12), 8169–8196. https://doi.org/10.1002/2015JB012292

Wakita, K. (2015). OPS mélange: A new term for mélanges of convergent margins of the world. *International Geology Review*, *57*(5–8), 529–539. https://doi.org/10.1080/00206814.2014.949312

Willner, A. P., Sepúlveda, F. A., Hervé, F., Massonne, H. J., & Sudo, M. (2009). Conditions and timing of pumpellyite-actinolite-facies metamorphism in the early mesozoic frontal accretionary prism of the madre de dios archipelago (Latitude 50°20′S; Southern Chile). *Journal of Petrology*, *50*(11), 2127–2155. https://doi.org/10.1093/petrology/egp071

Yamaguchi, A., Ujiie, K., Nakai, S., & Kimura, G. (2012). Sources and physicochemical characteristics of fluids along a subduction-zone megathrust: A geochemical approach using syn-tectonic mineral veins in the Mugi mélange, shimanto accretionary complex. *Geochemistry, Geophysics, Geosystems*, *13*(7), Q0AD24. https://doi.org/10.1029/2012GC004137

Yoshioka, S., Suminokura, Y., Matsumoto, T., & Nakajima, J. (2013). Two-dimensional thermal modeling of subduction of the Philippine Sea plate beneath southwest Japan. *Tectonophysics*, *608*, 1094–1108. https://doi.org/10.1016/j.tecto.2013.07.003

Zhang, L., He, C., Liu, Y., & Lin, J. (2017). Frictional properties of the South China Sea oceanic basalt and implications for strength of the Manila subduction seismogenic zone. *Marine Geology*, *394*, 16–29. https://doi.org/10.1016/j.margeo.2017.05.006